Supporting Information

The Electronic Nature of Cationic Group 10 Ylidyne Complexes

Leonard R. Maurer[1,3,†], Jens Rump[2,3,†] and Alexander C. Filippou[3,*]

[1] E-Mail: l.maurer@uni-bonn.de
[2] E-Mail: jens.rump@uni-bonn.de
[3] Institute of Inorganic Chemistry, University of Bonn, D-53121 Bonn, Germany
* Correspondence: filippou@uni-bonn.de
† Contributed equally to this work and are joint first authors

Table of Contents

1) Structural parameters of tetrylidyne complexes $[M{\equiv}E{-}R]^+$ and their metallotetrylene isomers $[M{-}\ddot{E}{-}R]^+$

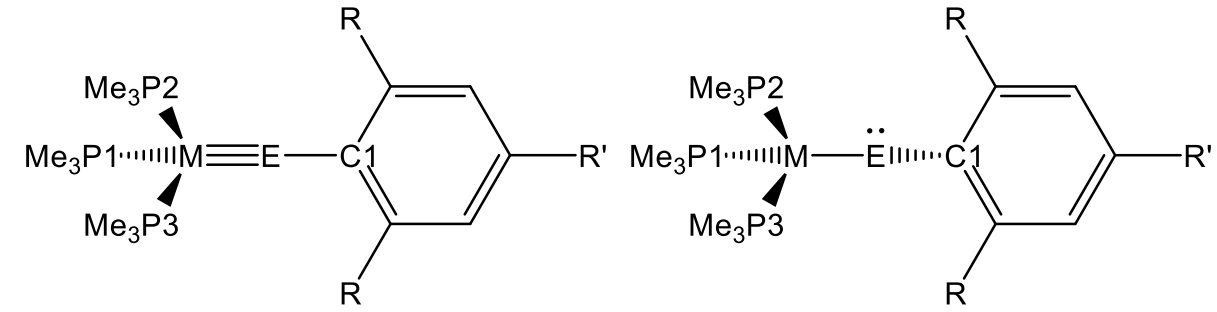

Figure S1. Lewis representations for the numbering of the tetrylidyne complexes and metallotetrylene isomers.

The geometry index τ_4 is used to distinguish whether the geometry of the coordination centre M is planar or tetrahedral. The formula is:

$$\tau_4 = \frac{\beta - \alpha}{360° - \vartheta} + \frac{180° - \beta}{180° - \vartheta}$$

where $\beta > \alpha$ are the two greatest valence angles of the coordination centre; $\vartheta = \cos^{-1}(-1/3) \approx 109.5°$ is a tetrahedral angle.[1] When τ_4 is close to 0 the structure is similar to square planar, while if τ_4 is close to 1 then the structure is similar to tetrahedral.

Table S1. Selected bond parameters of level of theory **I** optimized gas-phase structures (calc.) and structures obtained experimentally by single crystal X-ray diffraction (exp.) of group 10 tetrylidyne complexes. Bond lengths and angles are given in pm and deg, respectively.

compound	M−E	E−C1	M−E−C1	M−P1	M−P2	M−P3	τ_4
NiCAr^{Mes} (calc.)	169.1	141.3	168.4	221.9	224.5	226.4	0.80
NiSiTbb$_{exp}$ (exp.)	203.11(7)	183.8(2)	172.40(8)	218.96(8)	220.04(7)	220.54(8)	0.93
NiSiTbb (calc.)	204.5	184.0	167.2	219.8	221.7	221.9	0.92
NiSiAr^{Mes} (calc.)	204.2	186.6	163.8	219.0	221.9	222.4	0.90
NiGeAr$^{Mes}{}_{exp}$ (exp.)	210.40(6)	194.6(4)	164.9(2)	216.1(1)	220.3(1)	220.1(1)	0.91
	210.20(6)	195.0(4)	166.5(1)	218.1(1)	218.7(2)	220.4(1)	0.91
NiGeAr^{Mes} (calc.)	213.3	197.1	165.3	219.4	221.7	222.0	0.91
NiSnAr$^{Mes}{}_{exp}$ (exp.)	228.08(9)	214.0(5)	165.1(2)	233.9(4)[a]	220.8(3)[a]	212.7(4)[a]	0.90
				212.7(3)[a]	226.0(4)[a]	222.9(4)[a]	0.90
NiSnAr^{Mes} (calc.)	235.1	219.4	150.9	217.5	221.4	222.3	0.92
NiPbAr^{Mes} (calc.)	244.9	229.7	142.7	216.7	221.1	222.0	0.92
PdCAr^{Mes} (calc.)	182.0	140.9	168.4	235.2	237.7	239.8	0.77
PdSiTbb (calc.)	215.1	184.0	163.1	234.3	237.7	238.0	0.89
PdSiAr^{Mes} (calc.)	216.1	187.6	150.7	232.0	238.0	239.3	0.86
PdGeAr^{Mes} (calc.)	227.9	199.5	144.9	231.2	237.42	238.6	0.87
PdSnAr^{Mes} (calc.)	251.6	222.9	134.4	230.5	236.8	238.8	0.87
PdPbAr^{Mes} (calc.)	263.1	232.4	129.6	230.2	236.3	238.6	0.83
PtCAr^{Mes} (calc.)	179.9	141.2	175.1	235.4	236.3	237.8	0.79
PtSiTbb$_{exp}$ (exp.)	213.43(7)	184.2(3)	173.83(9)	231.81(8)	232.65(7)	232.81(8)	0.93
PtSiTbb (calc.)	215.8	183.8	168.1	232.3	234.8	234.7	0.90
PtSiAr^{Mes} (calc.)	215.7	186.3	166.1	231.4	234.6	235.4	0.88
PtGeAr$^{Mes}{}_{exp}$ (exp.)	222.42(7)	194.7(7)	161.8(2)	226.8(2)	232.3(2)	231.4(2)	0.89
	222.69(8)	195.2(7)	163.3(2)	228.8(2)	230.3(3)	232.2(2)	0.88
PtGeAr^{Mes} (calc.)	228.4	198.9	149.7	229.0	234.0	235.6	0.88
PtSnAr^{Mes} (calc.)	255.1	223.9	132.1	228.6	234.0	235.8	0.83
PtPbAr^{Mes} (calc.)	267.7	233.1	127.3	228.7	233.4	235.4	0.79

[a]: Due to structural disorder of the PMe_3 ligands the Ni-P bond lengths of **NiSnAr$^{Mes}{}_{exp}$** vary in a wide range and are inaccurate.

Table S2. Selected bond parameters of level of theory **I** optimized gas-phase (calc.) structures of group 10 metallotetrylenes. Bond lengths and angles are given in pm and deg, respectively.

compound	M–E	E–C1	M–E–C1	M–P1	M–P2	M–P3	τ_4
NiCAr^{Mes}-2 (calc.)	180.6	145.0	99.7	232.3	225.0	223.8	0.51
NiSiTbb-2 (calc.)	–	–	–	–	–	–	–
NiSiAr^{Mes}-2 (calc.)	–	–	–	–	–	–	–
NiGeAr^{Mes}-2 (calc.)	235.9	204.0	95.1	229.5	221.0	220.7	0.51
NiSnAr^{Mes}-2 (calc.)	256.3	224.3	96.0	226.8	219.2	219.5	0.54
NiPbAr^{Mes}-2 (calc.)	264.2	234.3	94.8	225.5	218.8	219.0	0.54
PdCAr^{Mes}-2 (calc.)	194.7	144.4	103.8	248.0	239.3	237.6	0.44
PdSiTbb-2 (calc.)	235.1	189.7	98.8	253.9	236.7	235.0	0.50
PdSiAr^{Mes}-2 (calc.)	232.4	191.0	87.9	248.6	237.0	235.9	0.61
PdGeAr^{Mes}-2 (calc.)	246.4	202.7	90.6	247.9	236.9	236.8	0.50
PdSnAr^{Mes}-2 (calc.)	270.3	223.6	93.1	246.7	234.6	234.9	0.44
PdPbAr^{Mes}-2 (calc.)	277.4	232.7	93.6	244.0	233.3	233.8	0.43
PtCAr^{Mes}-2 (calc.)	196.4	145.1	108.9	245.2	234.7	233.4	0.43
PtSiTbb-2 (calc.)	239.0	191.0	101.0	250.0	230.6	232.2	0.49
PtSiAr^{Mes}-2 (calc.)	238.1	192.5	100.0	249.0	232.2	232.0	0.42
PtGeAr^{Mes}-2 (calc.)	250.7	204.0	98.7	245.0	231.8	231.7	0.41
PtSnAr^{Mes}-2 (calc.)	274.3	225.4	96.9	243.1	231.4	231.4	0.42
PtPbAr^{Mes}-2 (calc.)	281.9	233.7	94.3	241.3	230.6	230.8	0.43

2) Influence of other levels of theory on the structures of **NiSiTbb**, **NiSnAr^{Mes}** and **PtGeAr^{Mes}**

Table S3. Selected bond parameters of the optimized gas-phase structures of **NiSiTbb**, **NiSnAr^{Mes}** and **PtGeAr^{Mes}** . Bond lengths and angles are given in pm and deg, respectively. The minimum nature of the TPSS- and PW6B95-optimized structures was not confirmed by successive numerical frequency calculations.

compound	**level of theory**	**M–E**	**E–C**	**M–E–C1**
NiSiTbb	B97-D3(BJ)-ATM/def2-TZVP	204.5	184.0	167.2
	TPSS-D3(BJ)-ATM/def2-TZVP	204.0	183.6	167.7
	PW6B95-D3(BJ)-ATM/def2-TZVP	201.2	182.6	165.2
NiSnAr^{Mes}	B97-D3(BJ)-ATM/def2-TZVP	235.1	219.4	150.9
	TPSS-D3(BJ)-ATM/def2-TZVP	232.4	217.4	149.3
	PW6B95-D3(BJ)-ATM/def2-TZVP	231.3	217.1	149.8
PtGeAr^{Mes}	B97-D3(BJ)-ATM/def2-TZVP	228.4	198.9	149.7
	TPSS-D3(BJ)-ATM/def2-TZVP	226.7	197.2	151.3
	PW6B95-D3(BJ)-ATM/def2-TZVP	225.4	196.2	150.2

3) Comparison of methods for treating relativistic effects

The compound that is influenced most by relativistic effects is presumed to be **PtPbAr^{Mes}** with two elements of the sixth period. As can be seen in Table S4 the differences in the structural parameters obtained by using ECPs and the ZORA method are small. It is expected that the more accurate ZORA method would improve the results, but this is outmatched here by the great cost/benefit ratio of the ECPs.

Table S4. Comparison of the structure of **PtPbAr^{Mes}** with electronic core potentials (ECP) or explicit relativistic treatment by the Zero Order Regular Approximation (ZERO) method. Bond lengths and angles are given in pm and deg, respectively.

PtPbAr^{Mes}	Pt–Pb	Pb–C1	Pt–P1	Pt–P2	Pt–P3	Pt–Pb–C1
ECP	267.7	233.1	235.4	228.7	233.4	127.3
ZORA	266.4	233.1	233.7	227.5	232.0	128.3

4) Calculated and experimental data of compounds **B-Ge** and **B-Sn**

Table S5. Comparison of selected structural parameters of theoretically and experimentally obtained structures of compounds **B-Ge** and **B-Sn**. The values for **B-E′** and **B-E$_{exp}$** were taken from ref. [2]. **B-Ge-PMe$_3$** refers to [(PMe$_3$)$_3$Ni≡GeN(Si^{i}Pr$_3$)(Dipp)]$^+$. Bond lengths and angles are given in pm and deg, respectively.

compound	level of theory	M–E	E–N	M–E–N
B-Ge-PMe$_3$	B97-D3(BJ)-ATM/def2-TZVP	214.2	184.9	163.7
B-Ge	B97-D3(BJ)-ATM/def2-TZVP	218.3	186.4	173.4
B-Ge′	ωB97XD/def2-SVP (Ni,Ge: def2-TZVPP)	212.7	181.0	174.3
B-Ge$_{exp}$		215.9(1)	185.3(2)	175.9
B-Sn	B97-D3(BJ)-ATM/def2-TZVP	239.6	209.1	167.8
B-Sn′	ωB97XD/def2-SVP (Ni,Sn: def2-TZVPP)	232.8	202.6	169.3
B-Sn$_{exp}$		235.5(1)	206.6(6)	173.7

5) Selected canonical MOs of compounds **MER**

In all following figures the isosurface value is set to 0.04 $e^{1/2}$ $Bohr^{-3/2}$ and hydrogen atoms are omitted for clarity. Due to the Tbb and Ar^{Mes} substituents enhancing the delocalized nature of the MOs, the same sets of orbitals could not be depicted for each compound equally. This, in contrast, is much more straightforward for the Pipek-Mezey localized MOs (*vide infra*).

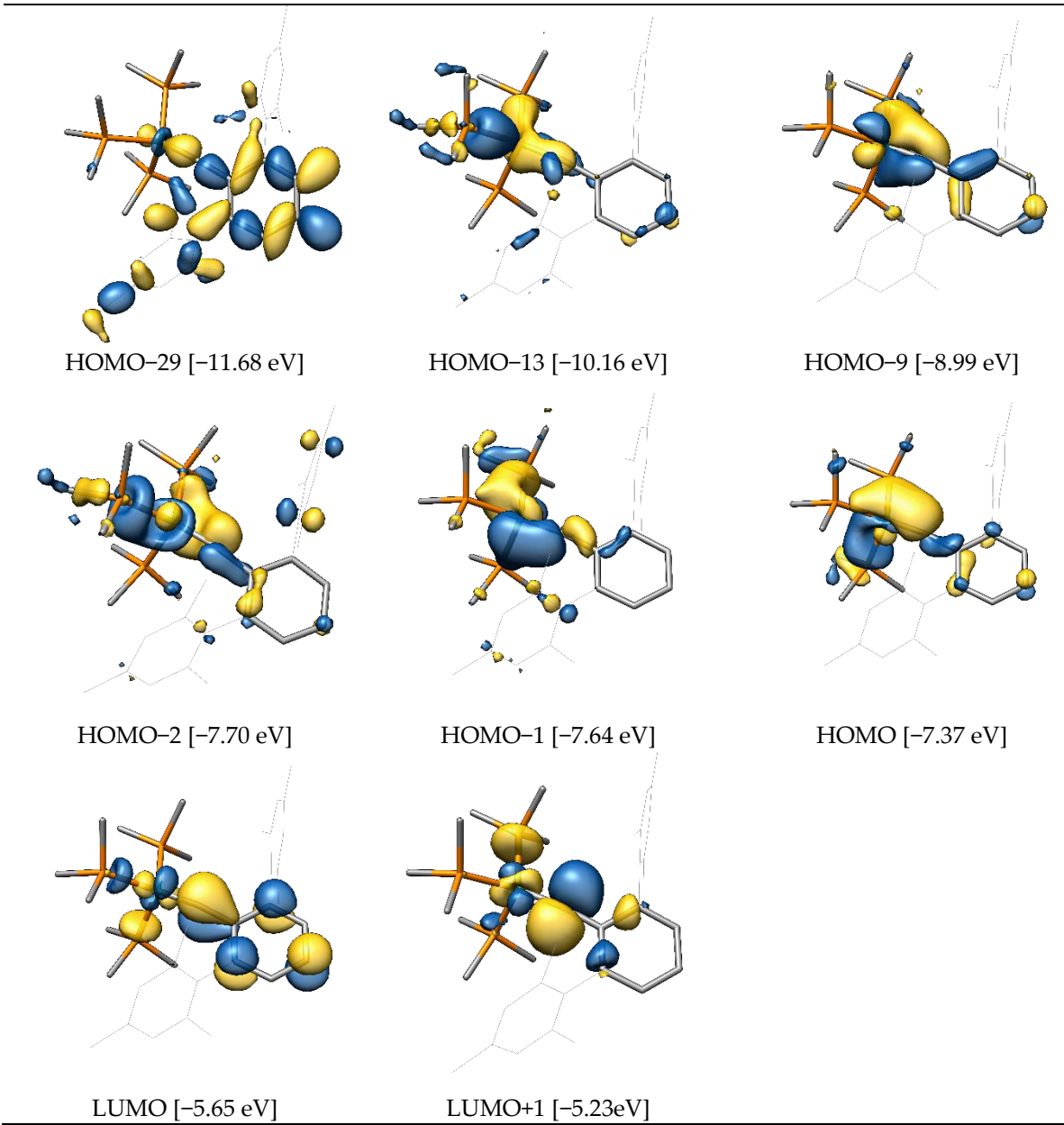

Figure S2. Selected canonical MOs of **NiCAr^{Mes}**.

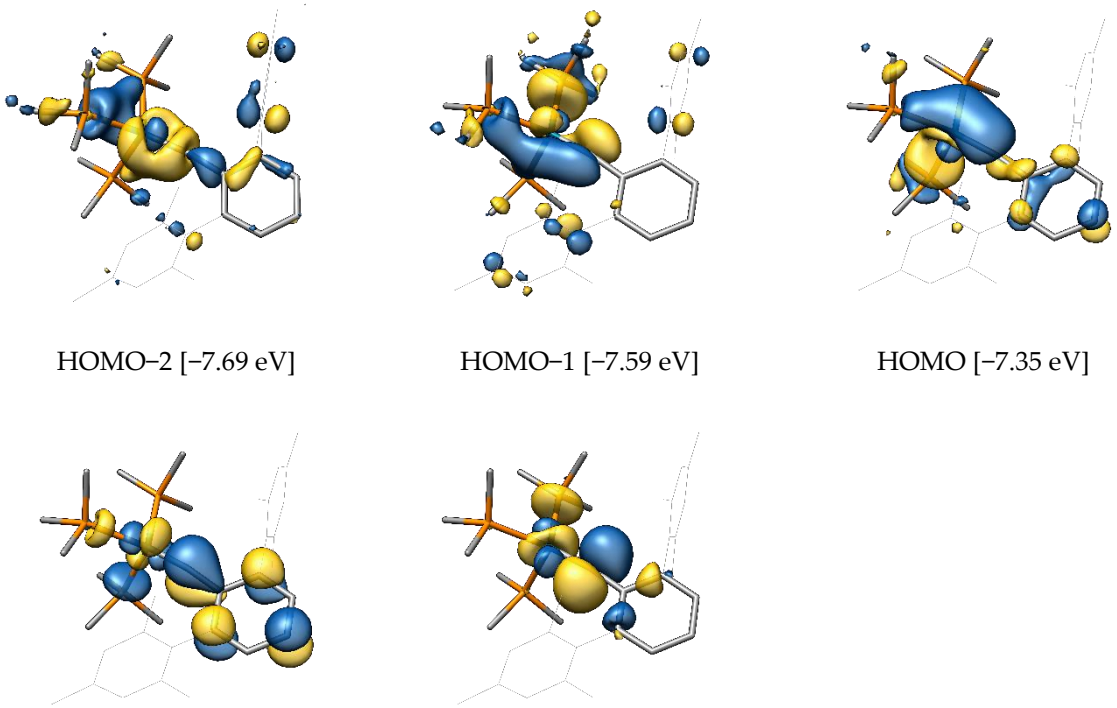

Figure S3. Selected canonical MOs of **PdCAr^{Mes}**.

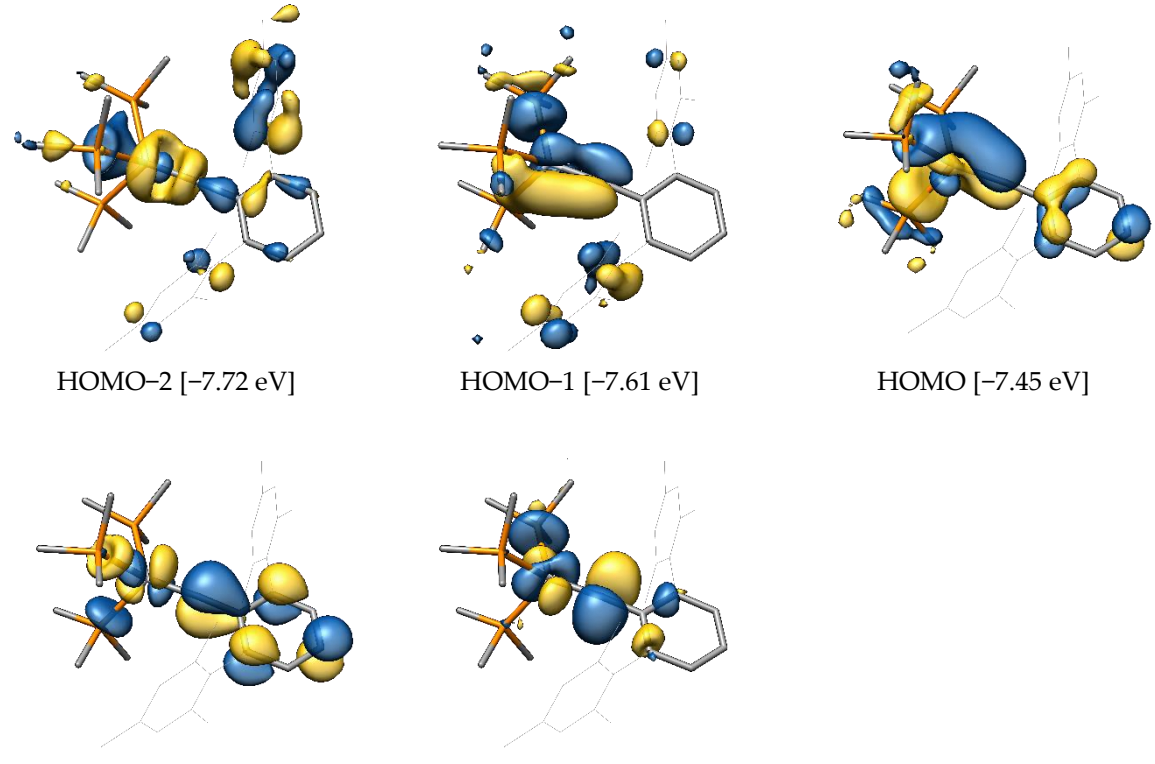

Figure S4. Selected canonical MOs of **PtCAr^{Mes}**.

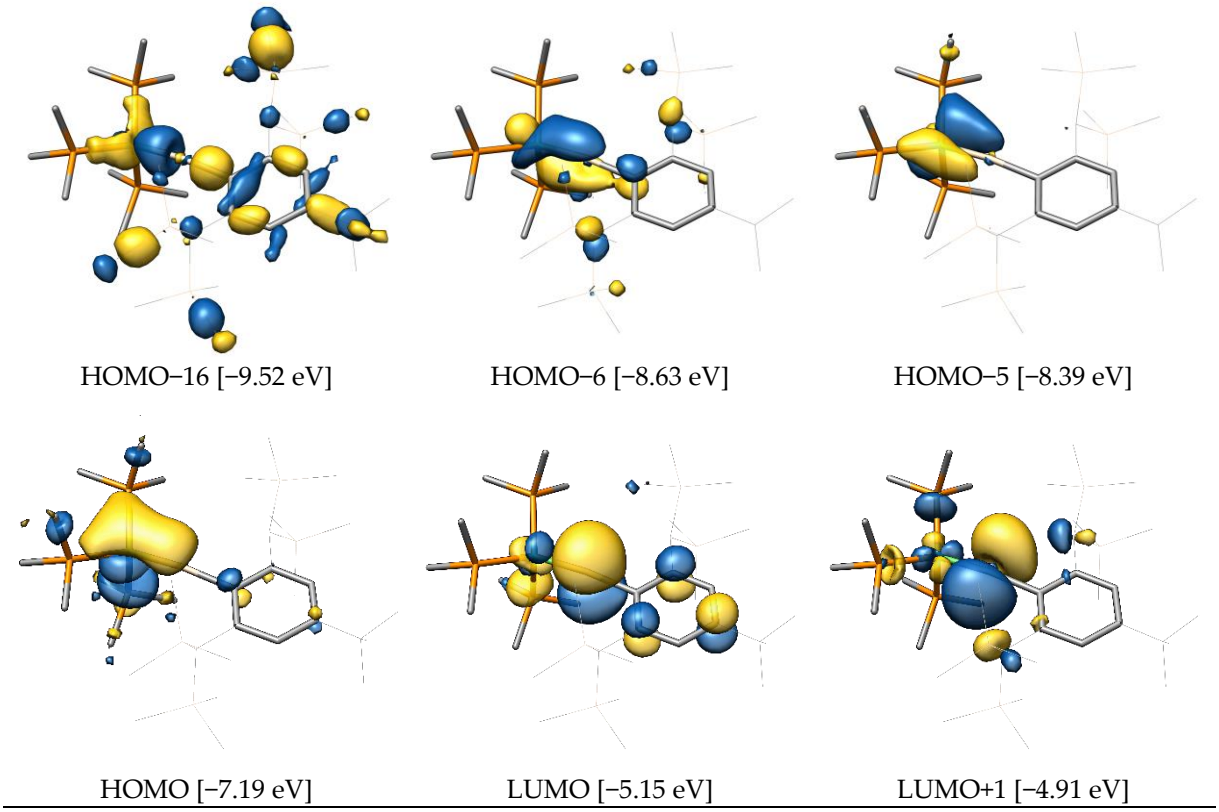

Figure S5. Selected canonical MOs of **NiSiTbb**.

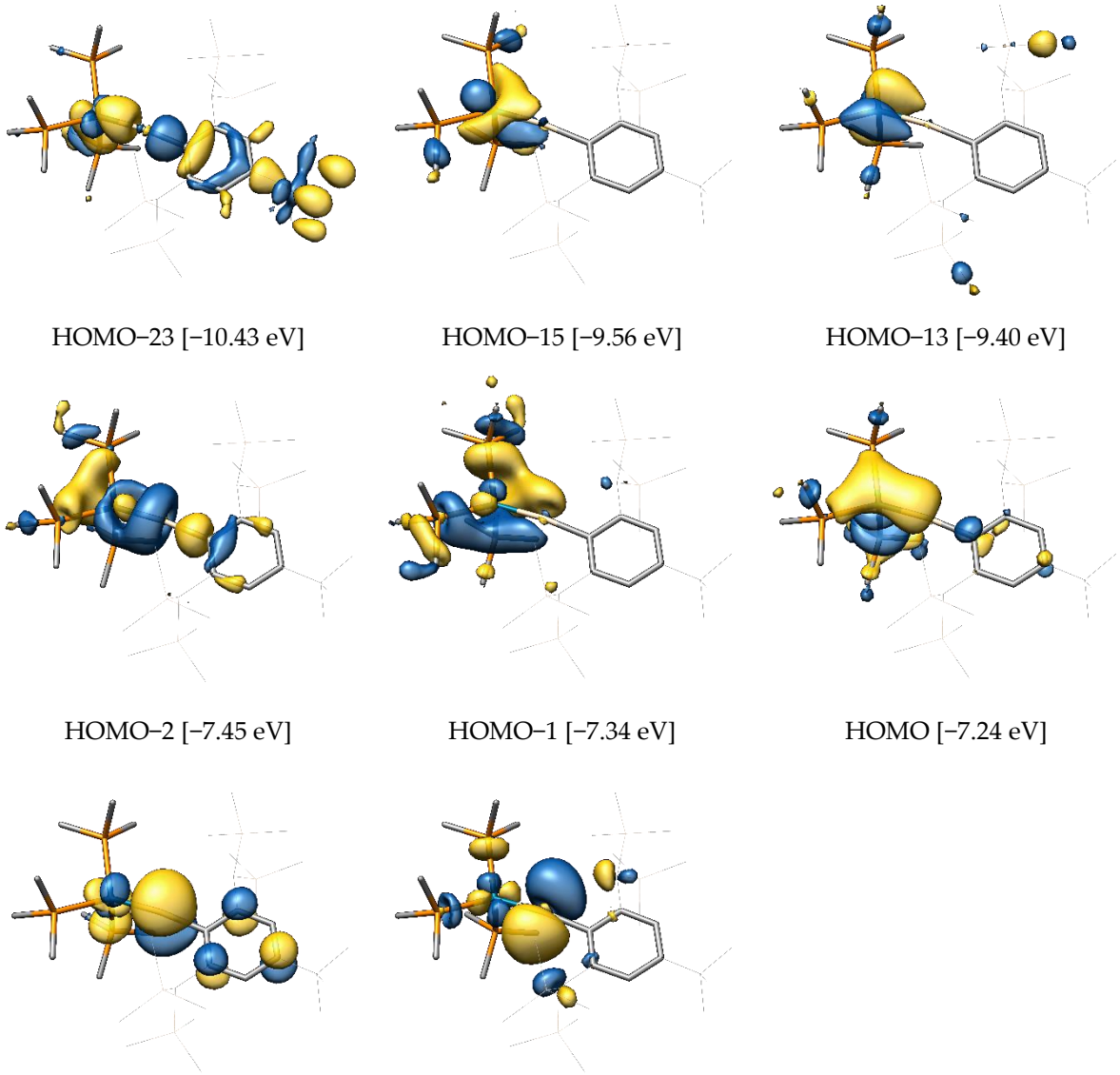

Figure S6. Selected canonical MOs of **PdSiTbb**.

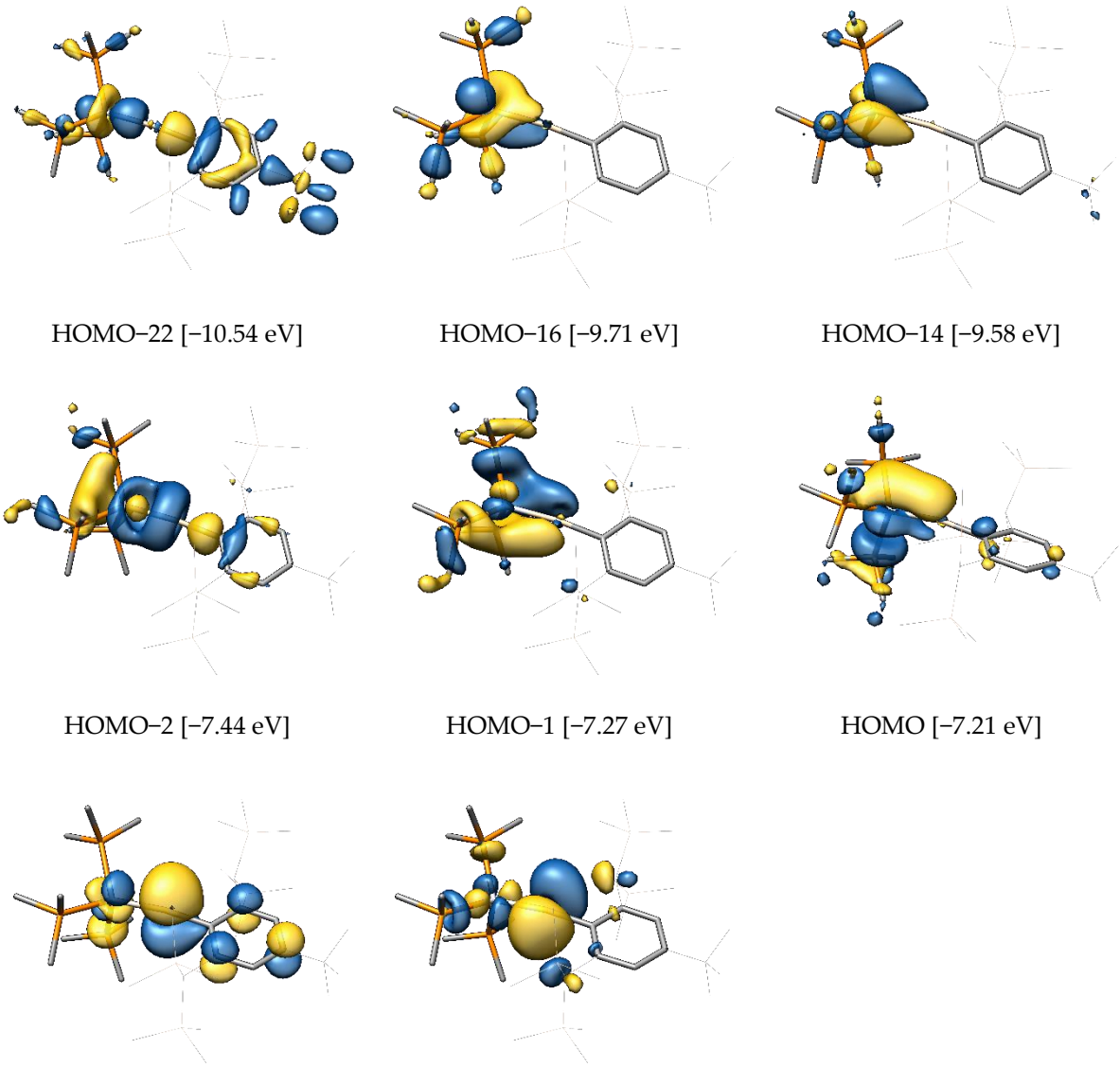

Figure S7. Selected canonical MOs of **PtSiTbb**. The HOMO is depicted in a slightly different perspective for better visibility of the orbital lobes.

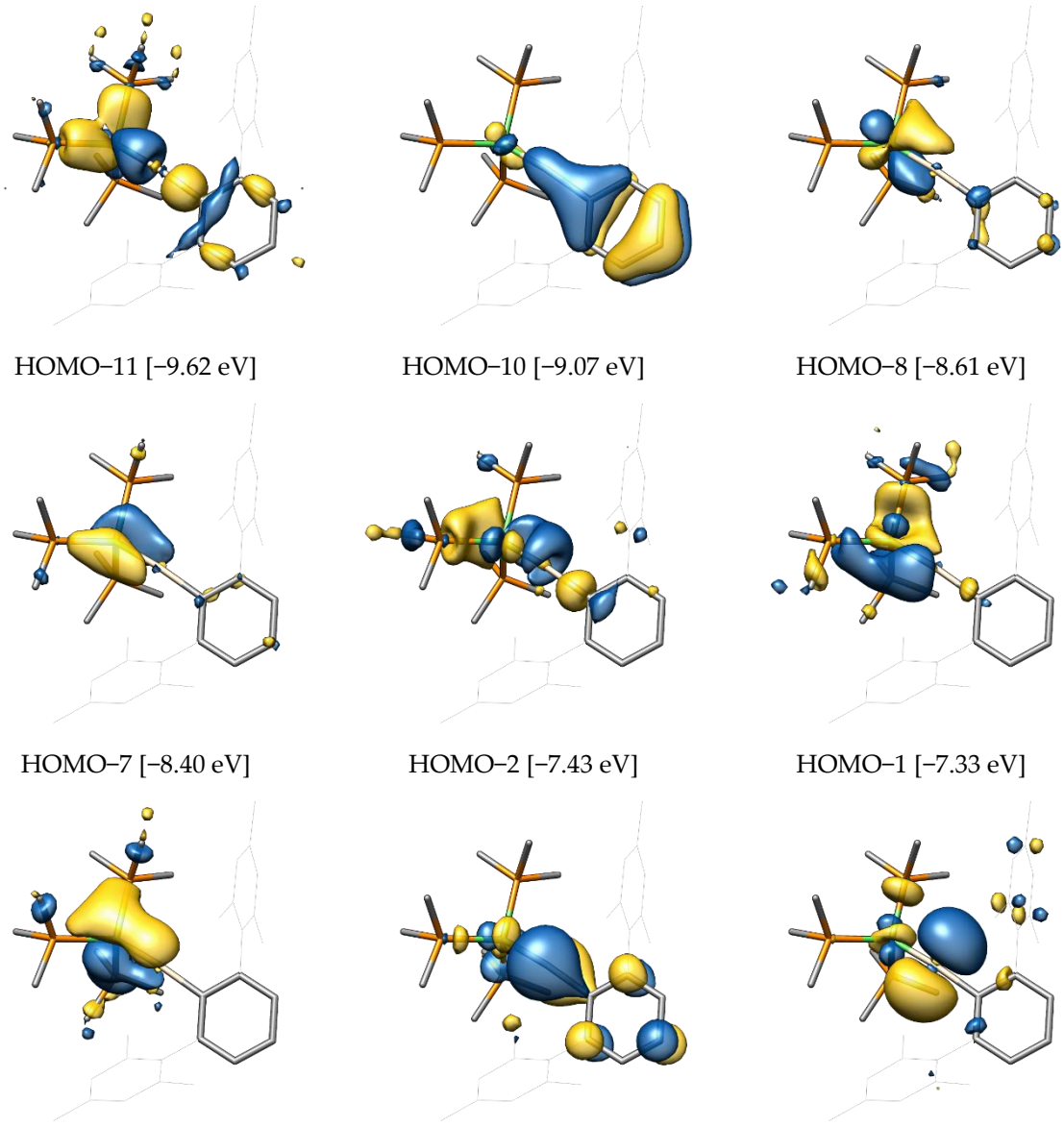

Figure S8. Selected canonical MOs of **NiSiAr^{Mes}**.

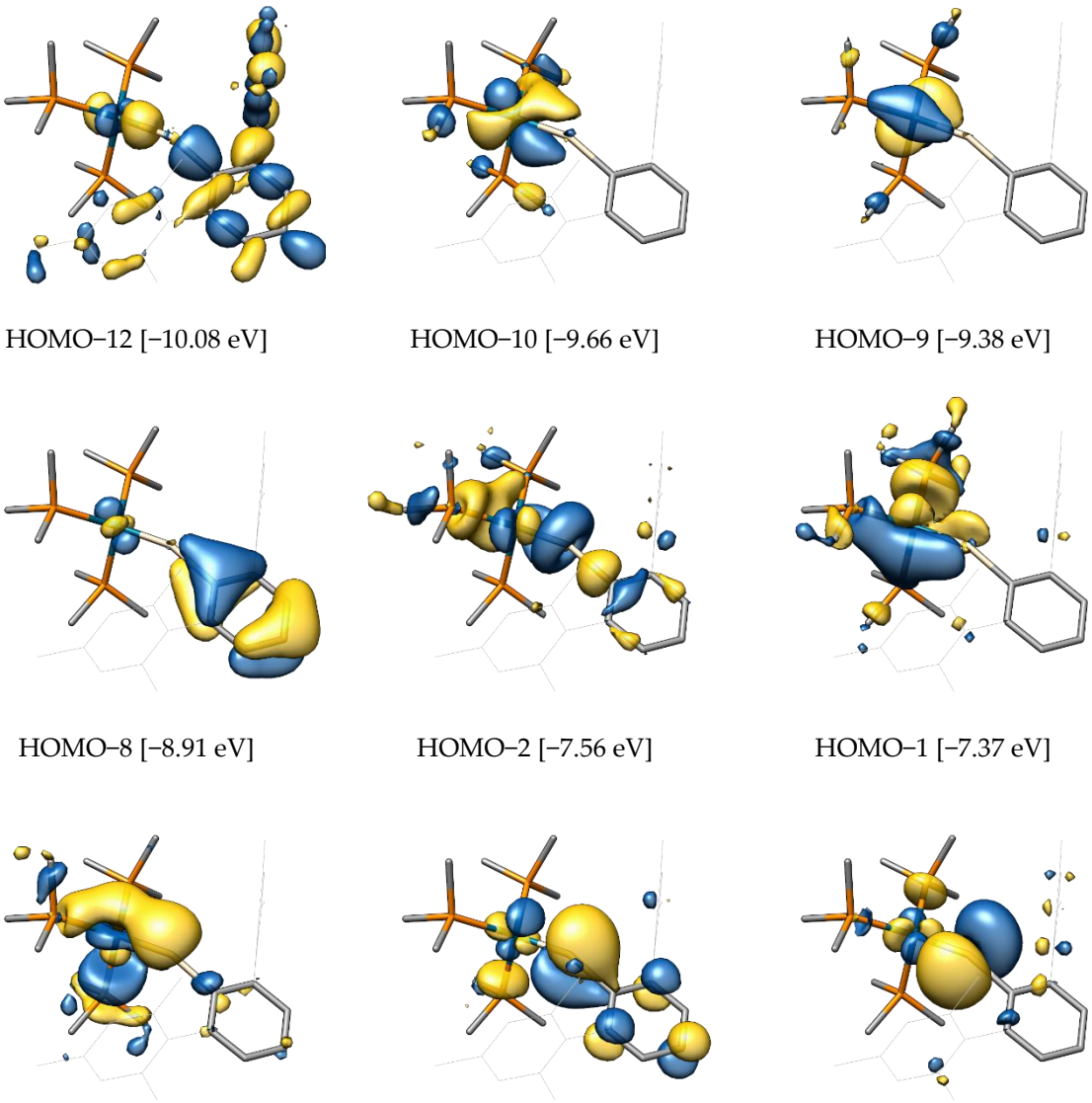

Figure S9. Selected canonical MOs of **PdSiAr^{Mes}**.

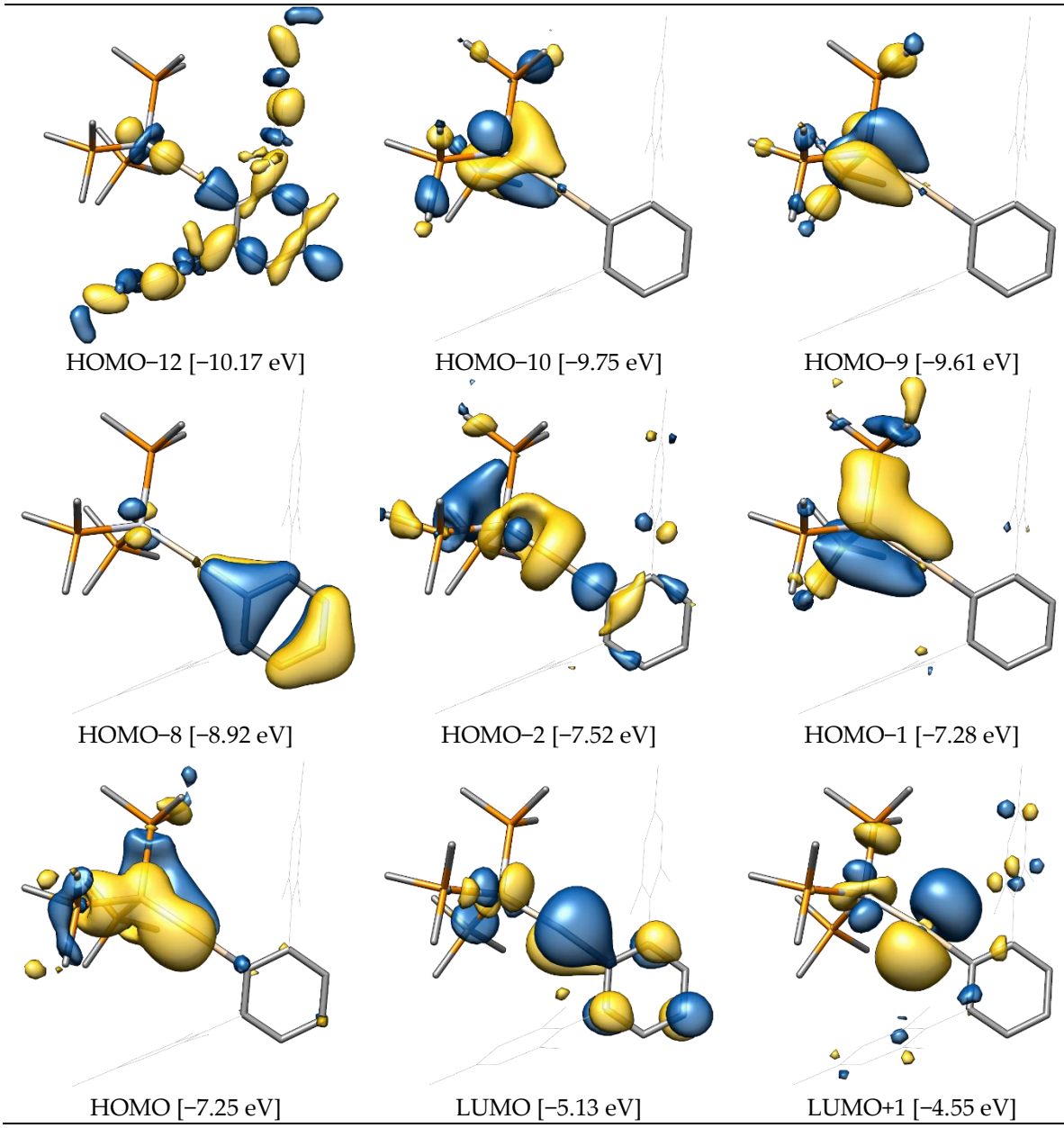

Figure S10. Selected canonical MOs of **PtSiAr^{Mes}**.

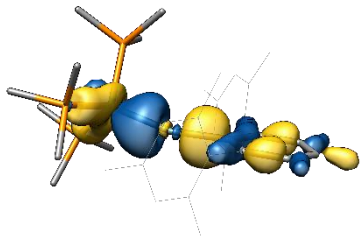

HOMO−11 [−9.51 eV]

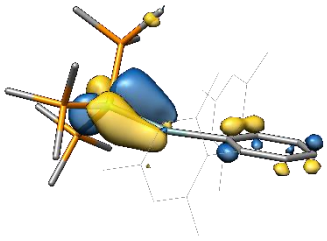

HOMO−8 [−8.49 eV]

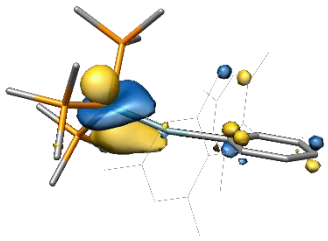

HOMO−7 [−8.33 eV]

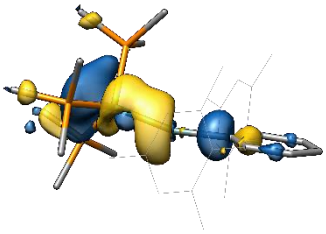

HOMO−2 [−7.41 eV]

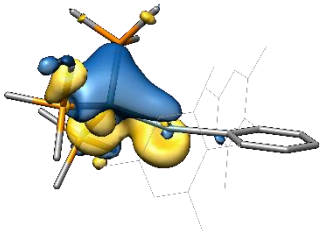

HOMO−1 [−7.30 eV]

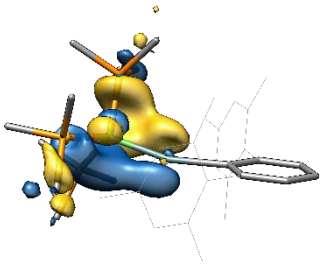

HOMO [−7.24 eV]

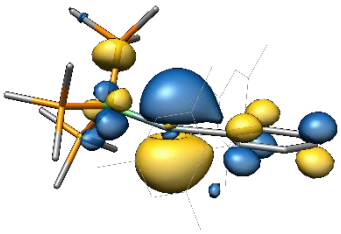

LUMO [−5.42 eV]

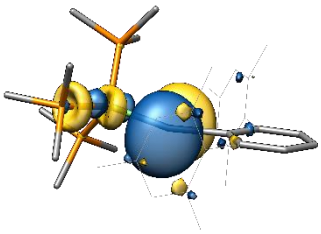

LUMO+1 [−5.05 eV]

Figure S11. Selected canonical MOs of **NiGeAr^{Mes}**. Although difficult to see, the non-bonding π(M–E)-type character in the HOMO is also present in the HOMO−1 and should not be mistaken for the π(M–E) bond.

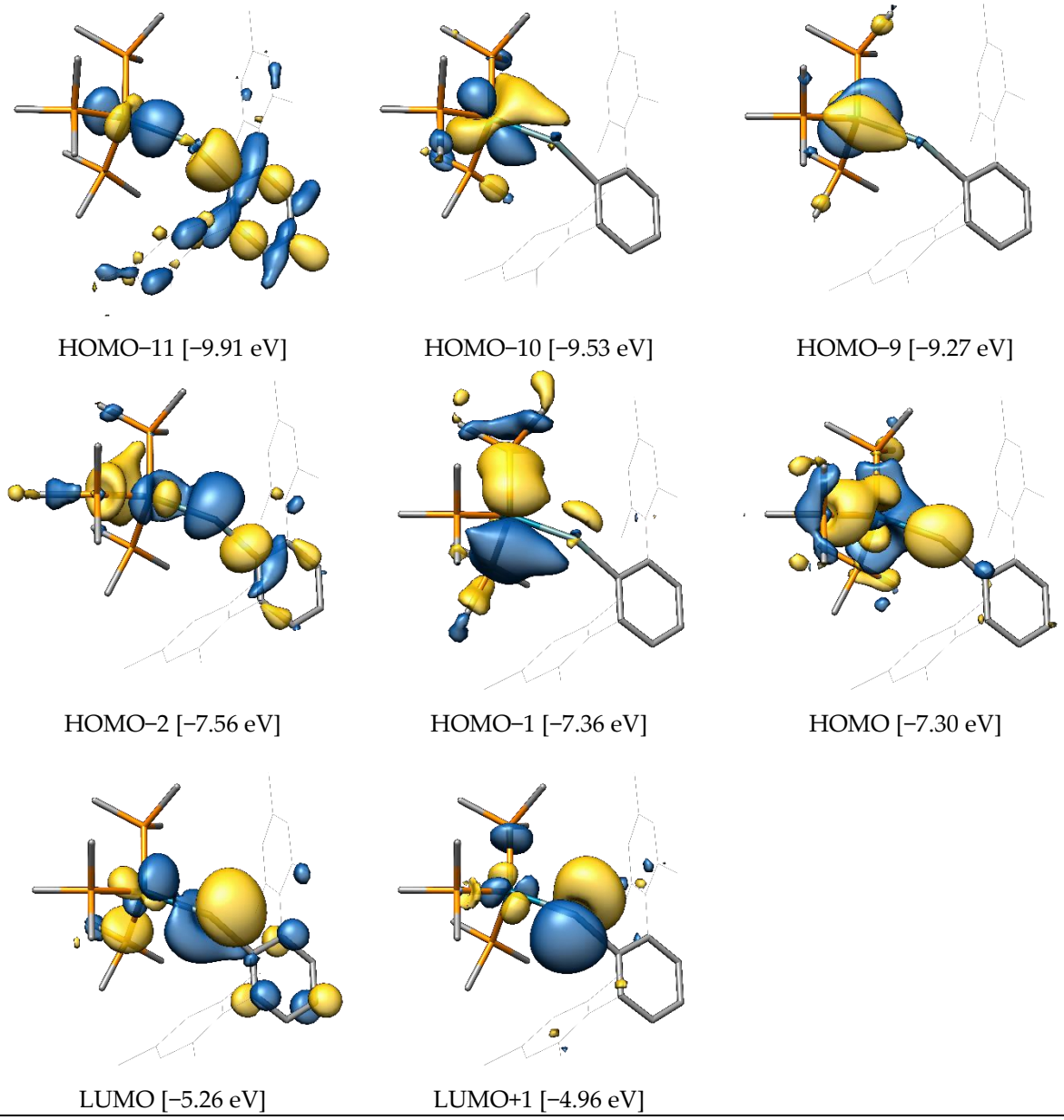

Figure S12. Selected canonical MOs of **PdGeAr^{Mes}**.

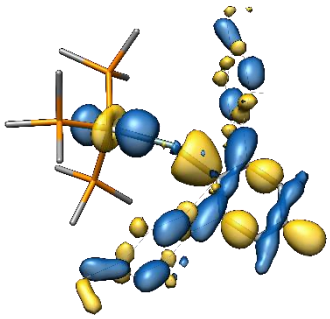

HOMO−12 [−10.03 eV]

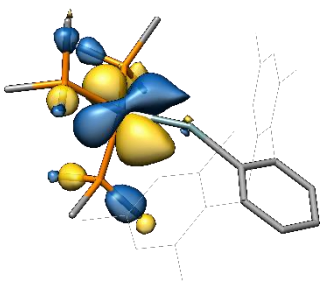

HOMO−10 [−9.71 eV]

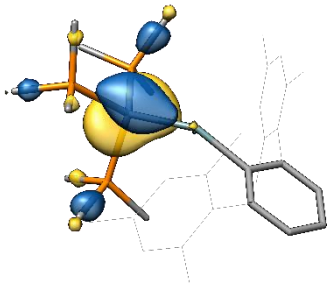

HOMO−9 [−9.49 eV]

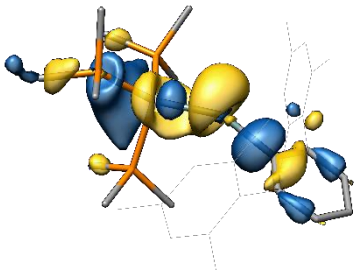

HOMO−2 [−7.50 eV]

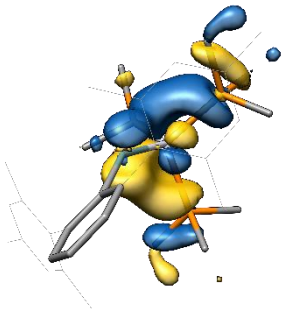

HOMO−1 [−7.32 eV]

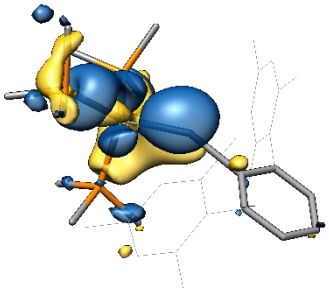

HOMO [−7.23 eV]

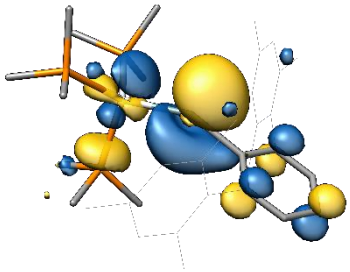

LUMO [−5.21 eV]

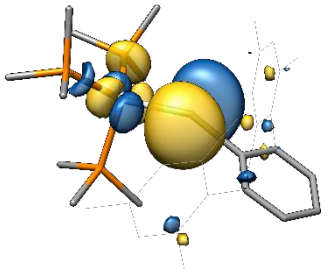

LUMO+1 [−4.72 eV]

Figure S13. Selected canonical MOs of **PtGeAr^{Mes}**. The HOMO−1 is depicted in a different perspective for better visibility of the orbital lobes.

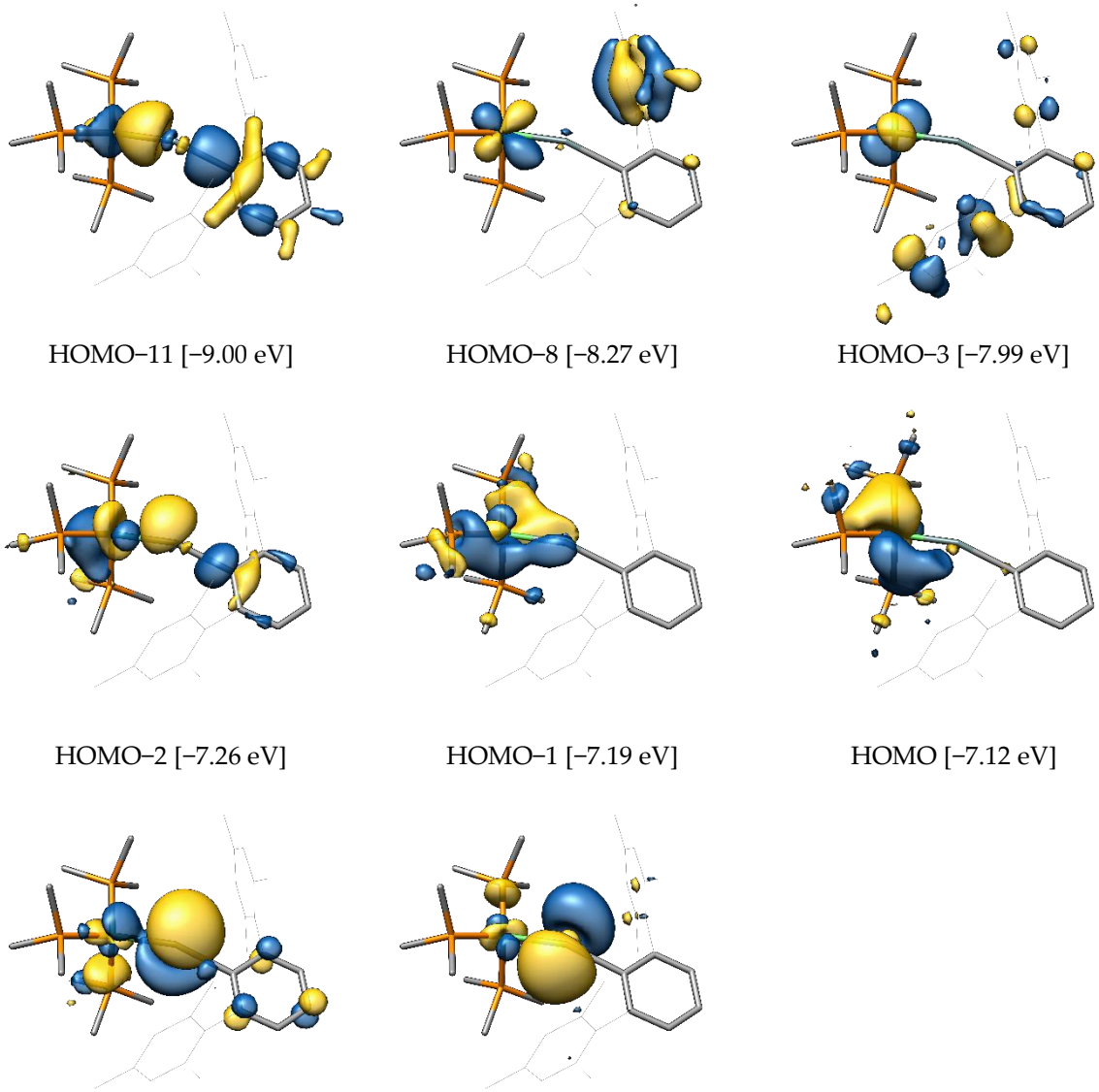

Figure S14. Selected canonical MOs of **NiSnAr^{Mes}**.

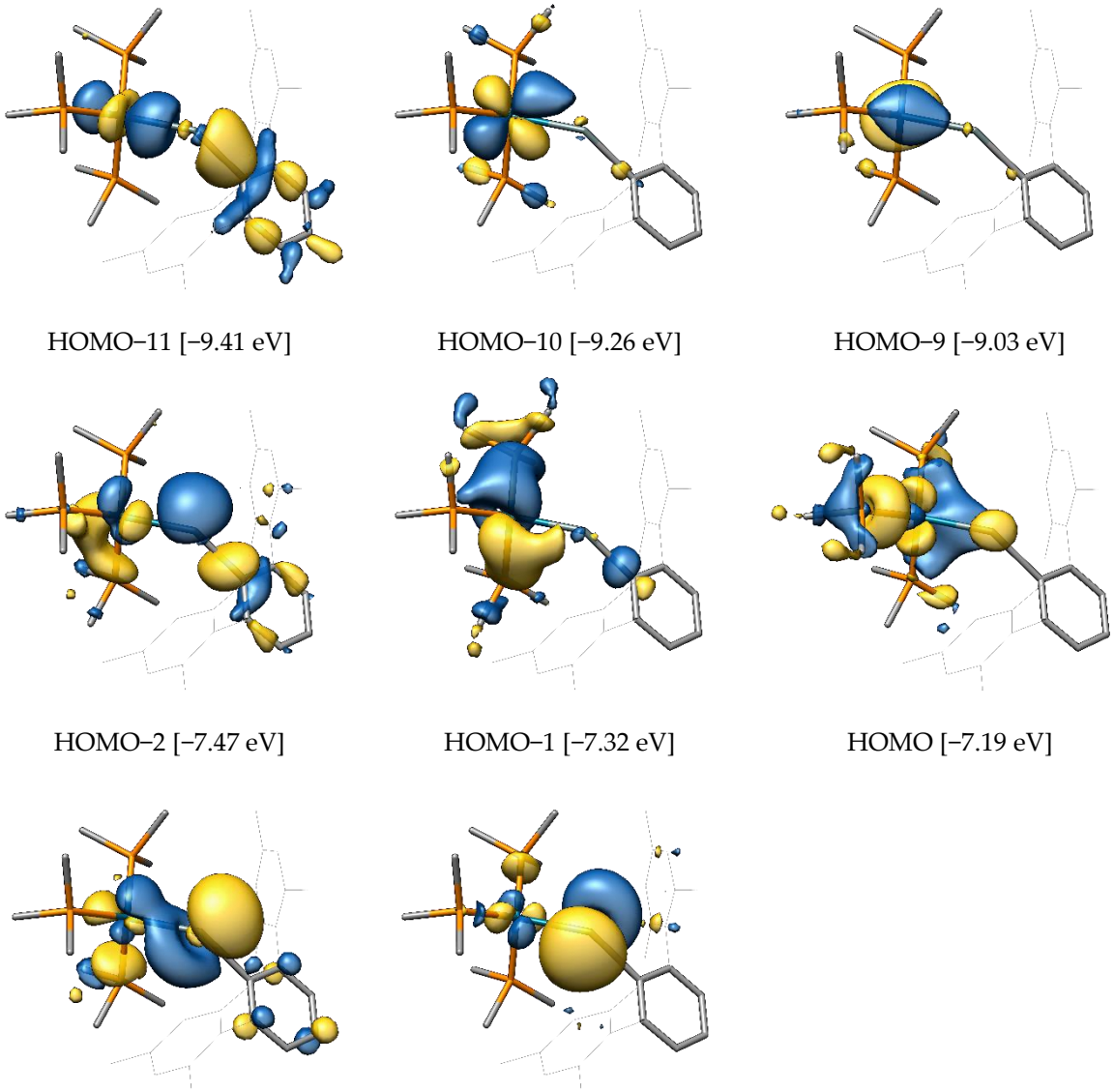

Figure S15. Selected canonical MOs of **PdSnAr^{Mes}**.

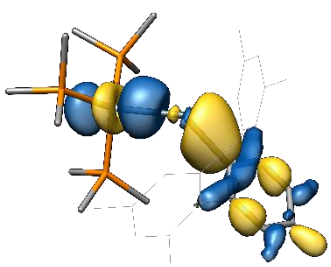

HOMO−11 [−9.53 eV]

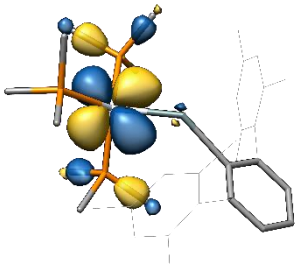

HOMO−10 [−9.44 eV]

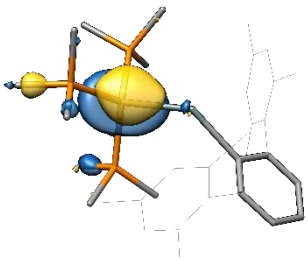

HOMO−9 [−9.19 eV]

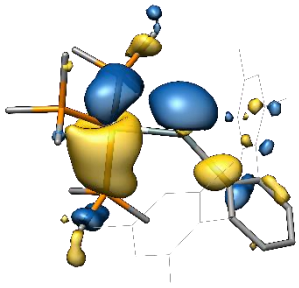

HOMO−2 [−7.53 eV]

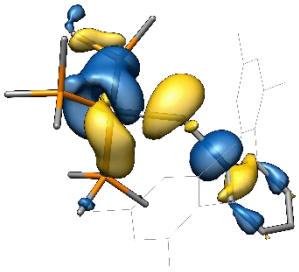

HOMO−1 [−7.30 eV]

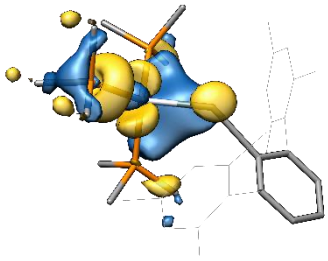

HOMO [−7.07 eV]

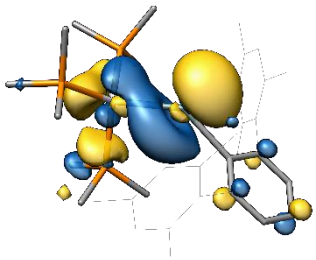

LUMO [−5.27 eV]

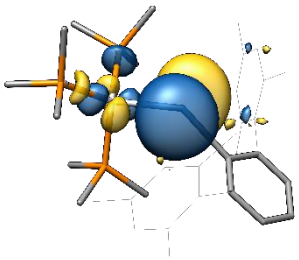

LUMO+1 [−4.85 eV]

Figure S16. Selected canonical MOs of **PtSnAr^{Mes}**.

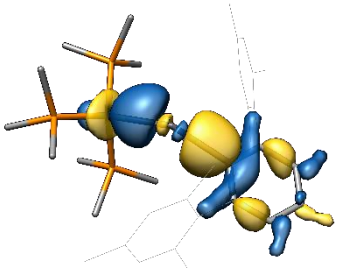

HOMO−11 [−8.74 eV]

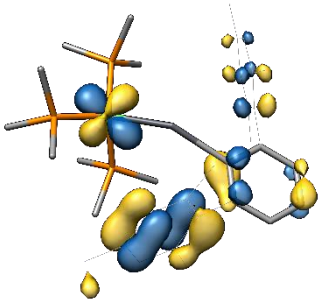

HOMO−5 [−8.06 eV]

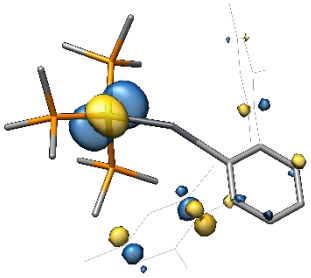

HOMO−3 [−7.87 eV]

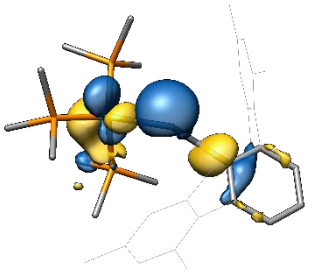

HOMO−2 [−7.21 eV]

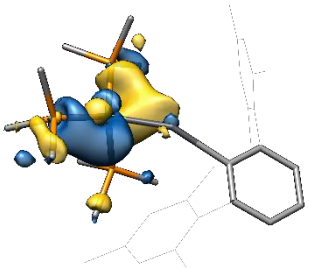

HOMO−1 [−7.15 eV]

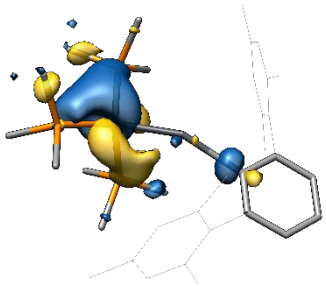

HOMO [−7.04 eV]

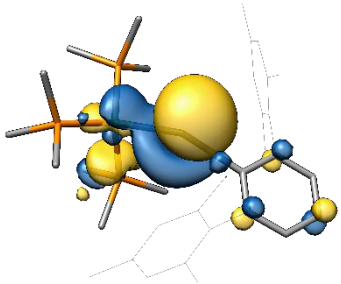

LUMO [−5.28 eV]

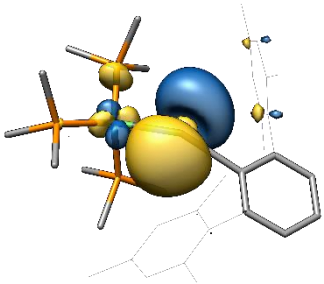

LUMO+1 [−4.98 eV]

Figure S17. Selected canonical MOs of **NiPbAr^{Mes}**.

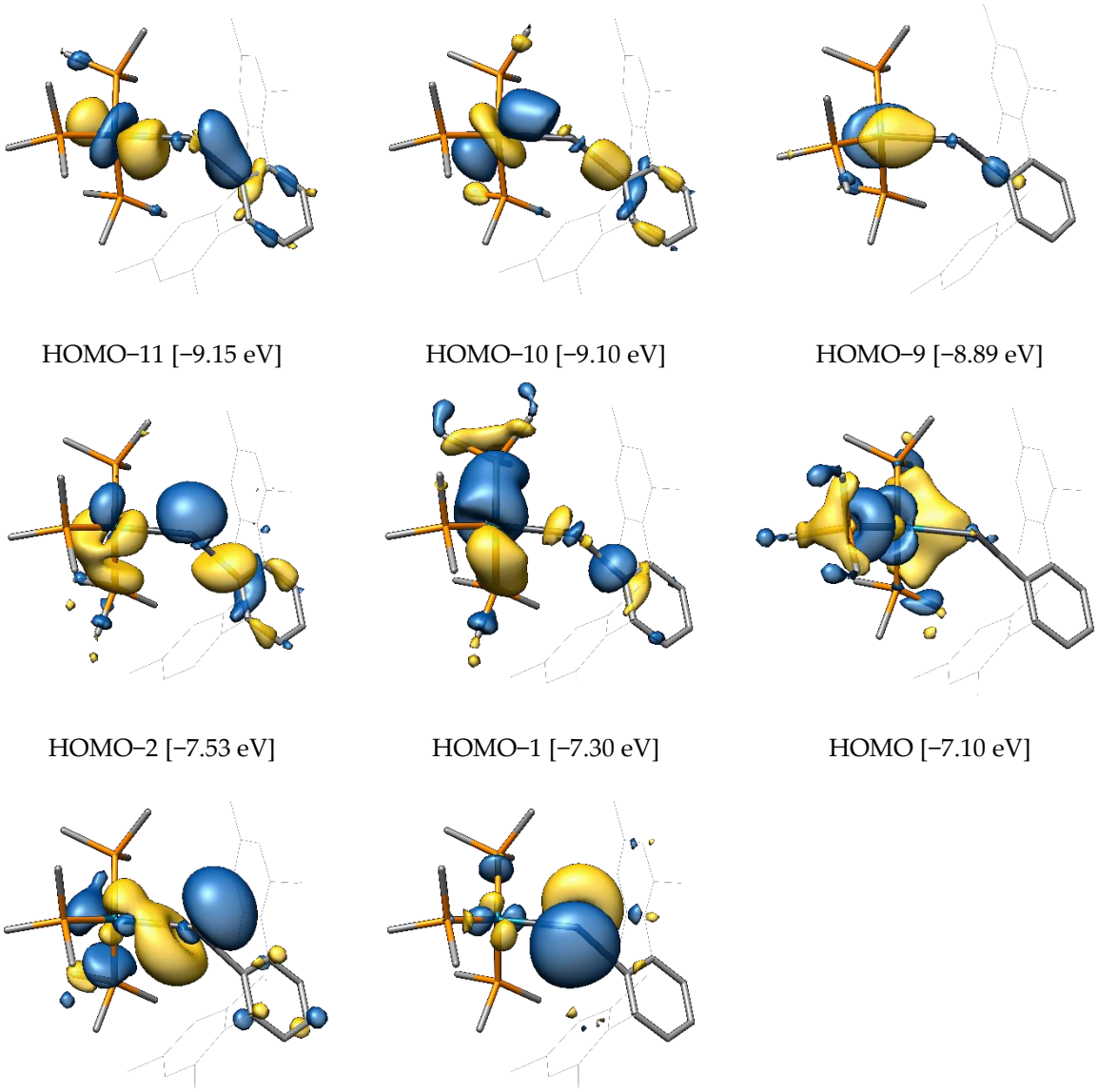

Figure S18. Selected canonical MOs of **PdPbAr^{Mes}**.

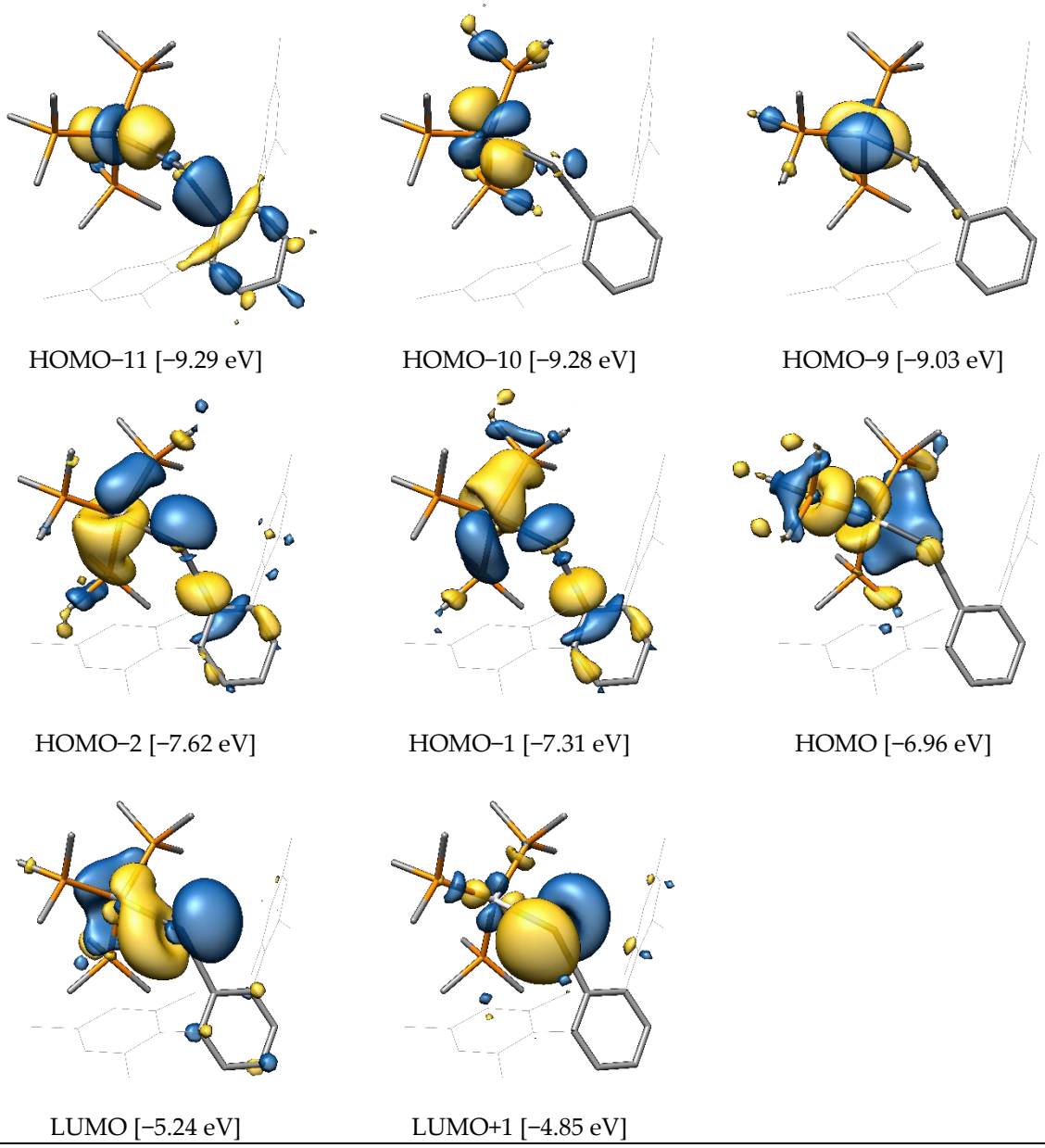

Figure S19. Selected canonical MOs of **PtPbAr^{Mes}**.

6) Selected Pipek-Mezey localized MOs of compounds **MER**

In all following figures the isosurface value is set to 0.04 $e^{1/2}$ $Bohr^{-3/2}$ and hydrogen atoms are omitted for clarity. For each localized MO, the attributed bond type and corresponding atomic Mulliken populations are also given.
The σ(M–P), σ(E–C) and π(E–C) as well as the three lone pair type orbitals d_1(M), d_2(M) and d_3(M) at the metal atom not used for π-bonding are plotted exemplary only for **NiSiTbb** and **PtPbAr^{Mes}** as they look very similar for all compounds, with only the participation of the E atom decreasing in the π(E–C) type LMO according to the Mulliken populations.

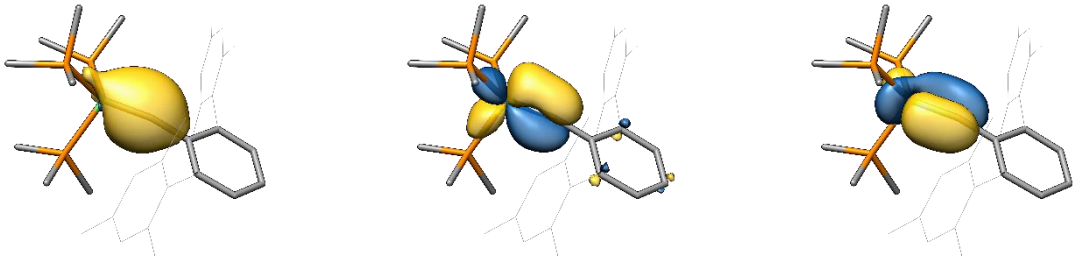

σ(Ni–C)	π_{xz}(Ni–C)	π_{yz}(Ni–C)
0.22 (Ni), 1.31 (C)	0.75 (Ni), 0.19 (C)	0.72 (Ni), 0.26 (C)

Figure S20. Selected Pipek-Mezey MOs of compound **NiCAr^{Mes}**.

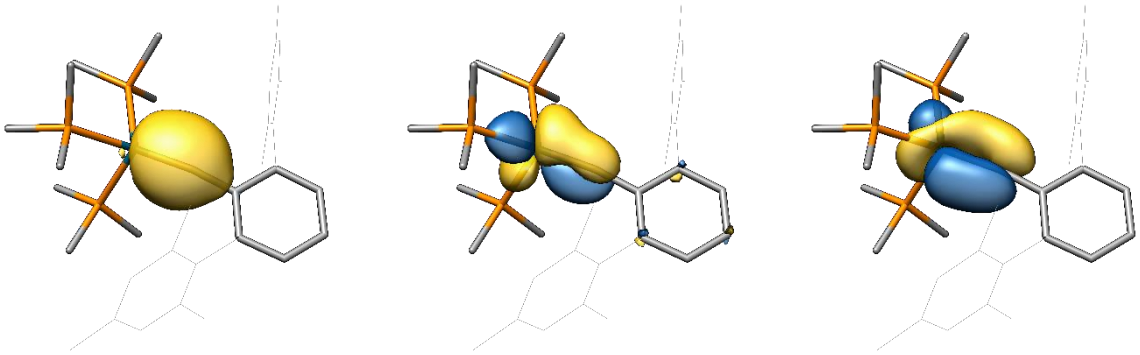

σ(Pd–C)	π_{xz}(Pd–C)	π_{yz}(Pd–C)
0.18 (Pd), 1.12 (C)	0.77 (Pd), 0.16 (C)	0.76 (Pd), 0.20 (C)

Figure S21. Selected Pipek-Mezey MOs of compound **PdCAr^{Mes}**.

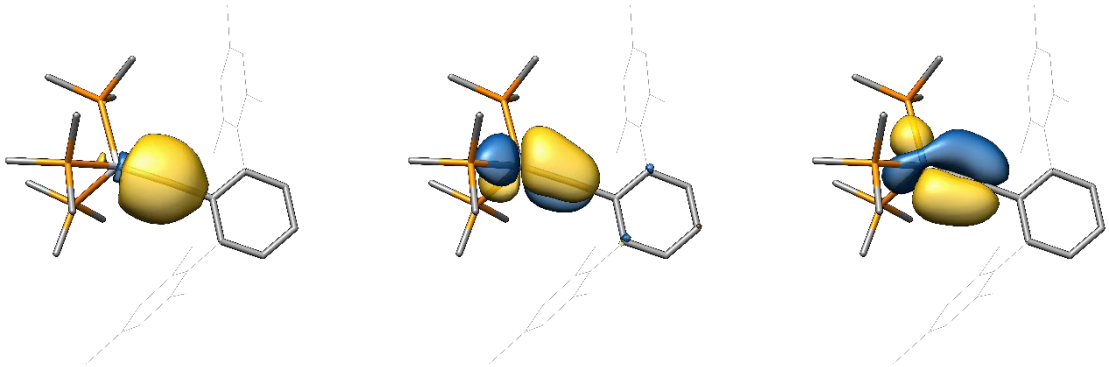

σ(Pt–C)	π_{xz}(Pt–C)	π_{yz}(Pt–C)
0.25 (Pt), 1.30 (C)	0.74 (Pt), 0.21 (C)	0.72 (Pt), 0.26 (C)

Figure S22. Selected Pipek-Mezey MOs of compound **PtCAr^{Mes}**.

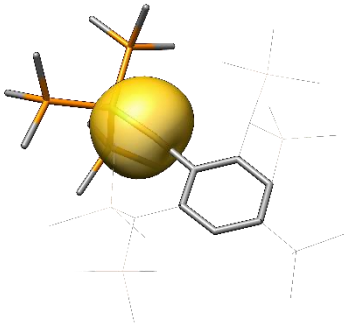

σ(Ni–Si)
0.19 (Ni), 0.80 (Si)

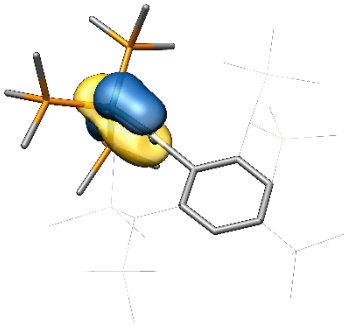

π_{xz}(Ni–Si)
0.81 (Ni), 0.19 (Si)

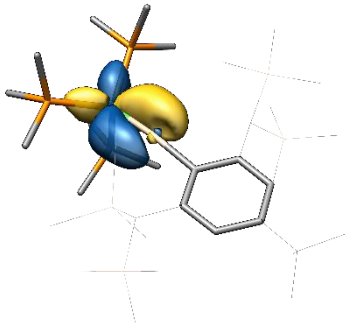

π_{yz}(Ni–Si)
0.79 (Ni), 0.19 (Si)

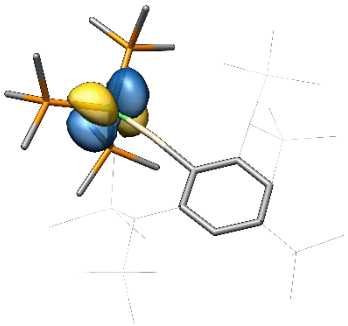

d_{xy}(Ni)
0.93 (Ni), 0.00 (Si)

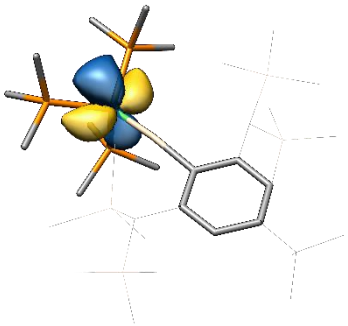

$d_{x^2-y^2}$(Ni)
0.93 (Ni), 0.00 (Si)

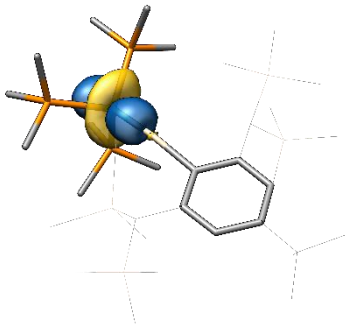

d_{z^2}(Ni)
0.93 (Ni), 0.04 (Si)

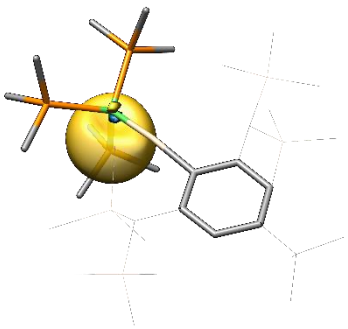

σ(Ni–P1)
0.82 (P1), 0.13 (Ni)

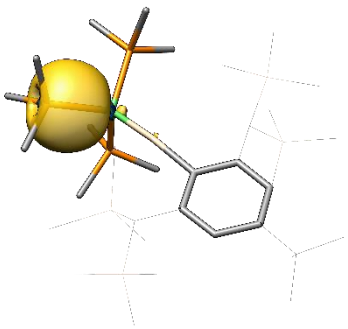

σ(Ni–P2)
0.83 (P2), 0.14 (Ni)

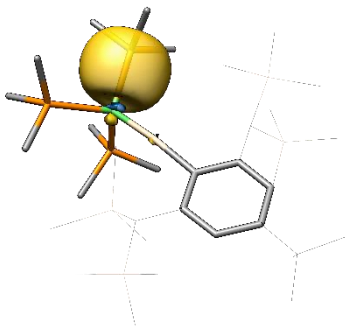

σ(Ni–P3)
0.81 (P3), 0.13 (Ni)

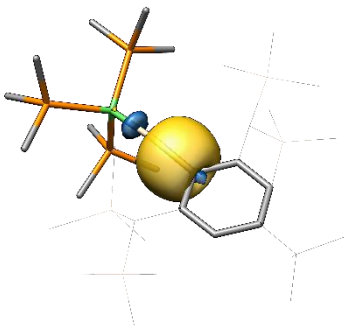

σ(Si–C1)
0.42 (Si), 0.74 (C1)

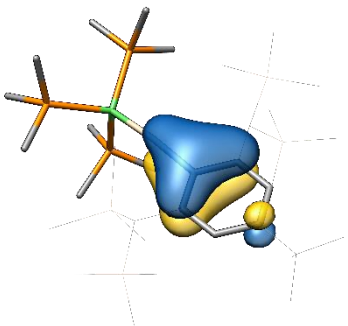

π(Si–C1)
0.11 (Si), 0.52 (C1),
0.15 (C_o), 0.18 (C_o')

Figure S23. Selected Pipek-Mezey MOs of compound **NiSiTbb**. C_o = ortho carbon atoms of the phenyl substituent.

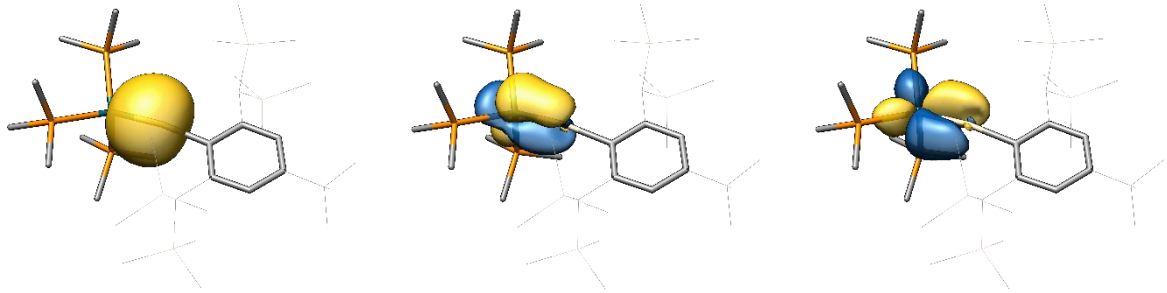

σ(Pd–Si)	π_{xz}(Pd–Si)	π_{yz}(Pd–Si)
0.15 (Pd), 0.86 (Si)	0.83 (Pd), 0.13 (Si)	0.83 (Pd), 0.14 (Si)

Figure S24. Selected Pipek-Mezey MOs of compound **PdSiTbb**.

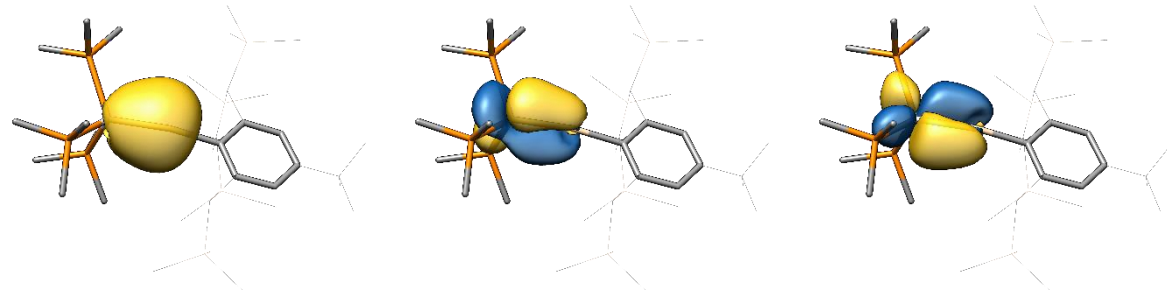

σ(Pt–Si)	π_{xz}(Pt–Si)	π_{yz}(Pt–Si)
0.13 (Pt), 0.87 (Si)	0.81 (Pt), 0.14 (Si)	0.80 (Pt), 0.17 (Si)

Figure S25. Selected Pipek-Mezey MOs of compound **PtSiTbb**.

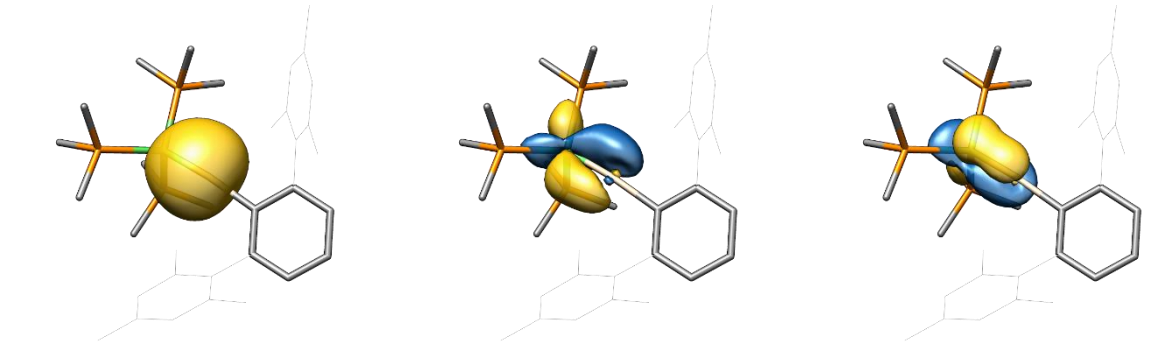

σ(Ni–Si)	π_{yz}(Ni–Si)	π_{xz}(Ni–Si)
0.20 (Ni), 0.81 (Si)	0.80 (Ni), 0.17 (Si)	0.80 (Ni), 0.16 (Si)

Figure S26. Selected Pipek-Mezey MOs of compound **NiSiAr^{Mes}**.

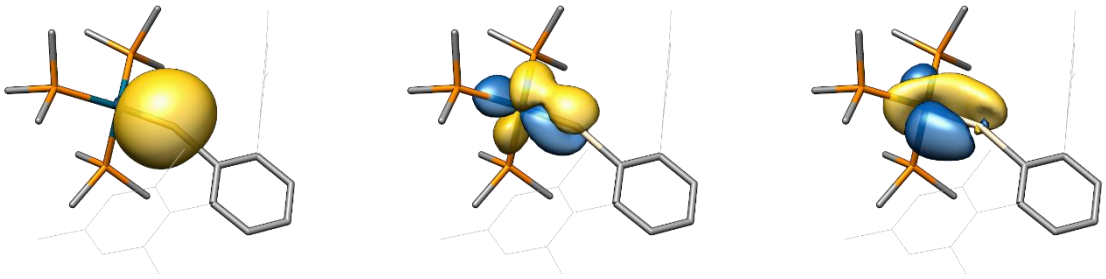

σ(Pd–Si)	π_{xz}(Pd–Si)	π_{yz}(Pd–Si)
0.88 (Si)	0.82 (Pd), 0.15 (Si)	0.84 (Pd), 0.13 (Si)

Figure S27. Selected Pipek-Mezey MOs of compound **PdSiAr^{Mes}**.

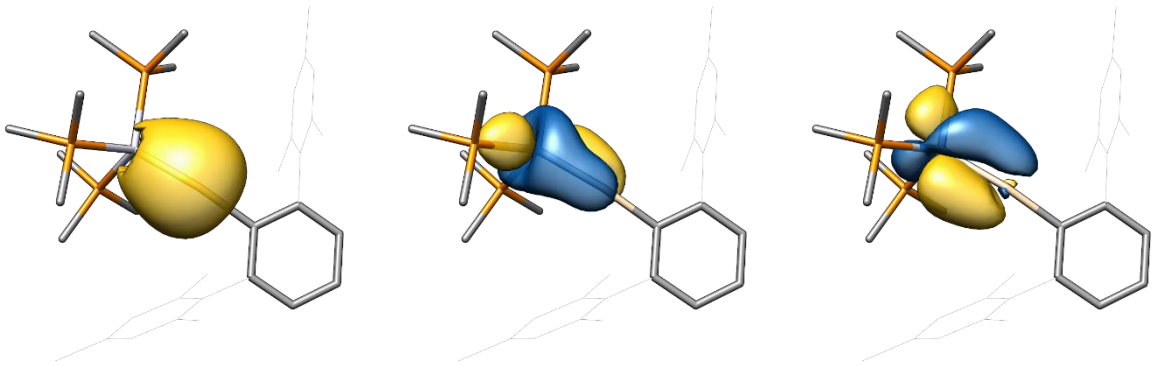

σ(Pt–Si)	π_{yz}(Pt–Si)	π_{xz}(Pt–Si)
0.14 (Pt), 0.88 (Si)	0.79 (Pt), 0.16 (Si)	0.81 (Pt), 0.15 (Si)

Figure S28. Selected Pipek-Mezey MOs of compound **PtSiAr^{Mes}**.

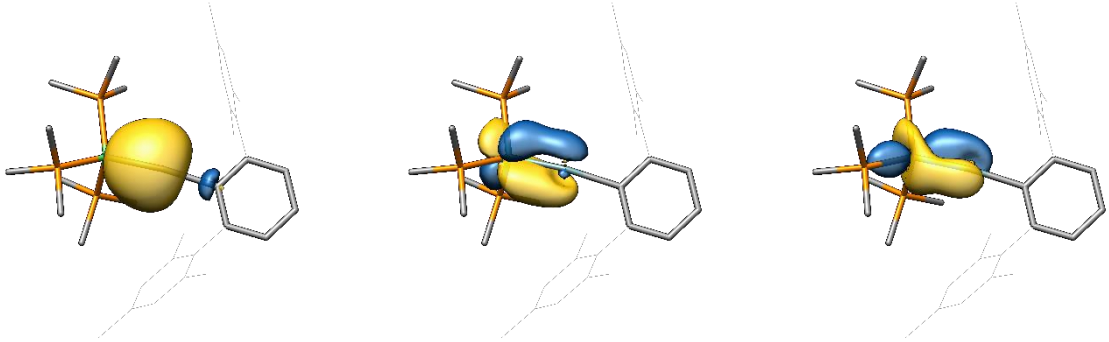

σ(Ni–Ge)	π_{xz}(Ni–Ge)	π_{yz}(Ni–Ge)
0.21 (Ni), 0.70 (Ge)	0.80 (Ni), 0.16 (Ge)	0.81 (Ni), 0.15 (Ge)

Figure S29. Selected Pipek-Mezey MOs of compound **NiGeAr^{Mes}**.

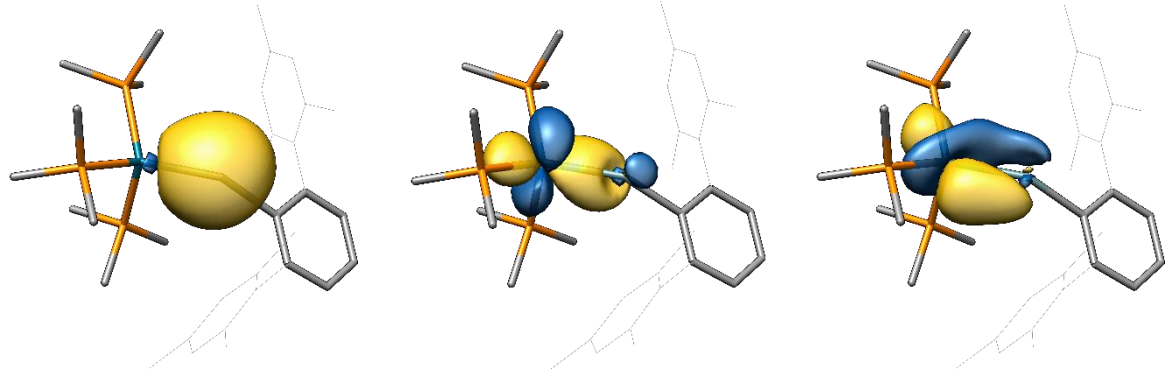

σ(Pd–Ge)	π_{xz}(Pd–Ge)	π_{yz}(Pd–Ge)
0.16 (Pd), 0.89 (Ge)	0.82 (Pd), 0.13 (Ge)	0.85 (Pd), 0.11 (Ge)

Figure S30. Selected Pipek-Mezey MOs of compound **PdGeAr^{Mes}**. Due to the M–E–C bending, the π_{xz}(Pd–Ge) orbital appears distorted.

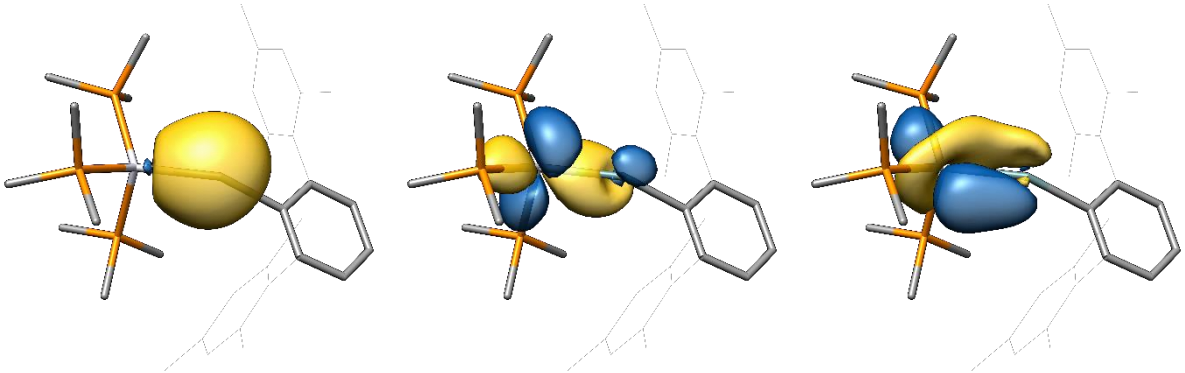

σ(Pt–Ge)	π_{xz}(Pt–Ge)	π_{yz}(Pt–Ge)
0.05 (Pt), 0.92 (Ge)	0.80 (Pt), 0.14 (Ge)	0.83 (Pt), 0.12 (Ge)

Figure S31. Selected Pipek-Mezey MOs of compound **PtGeAr^{Mes}**.

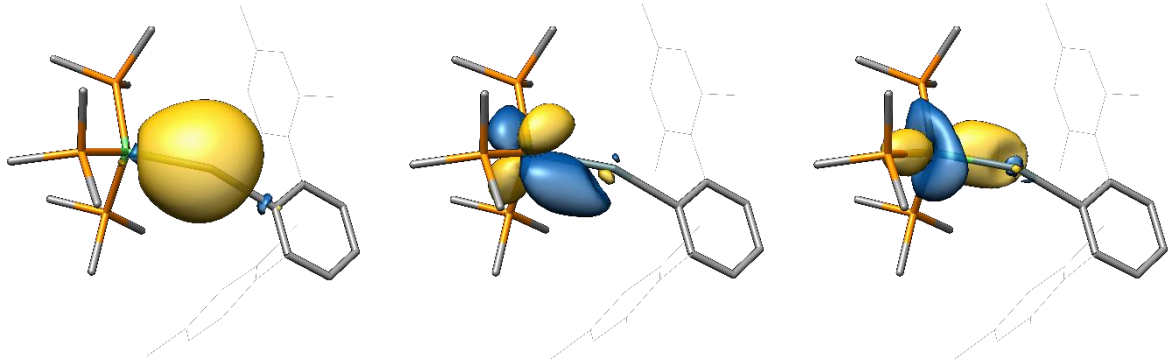

σ(Ni–Sn)	π_{xz}(Ni–Sn)	π_{yz}(Ni–Sn)
0.13 (Ni), 0.85 (Sn)	0.84 (Ni), 0.11 (Sn)	0.83 (Ni), 0.11 (Sn)

Figure S32. Selected Pipek-Mezey MOs of compound **NiSnAr^{Mes}**.

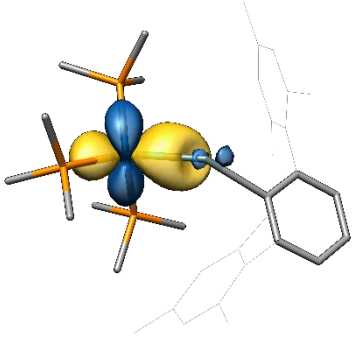

σ(Pd–Sn)
0.85 (Pd), 0.11 (Sn)

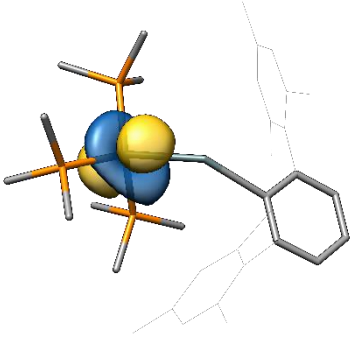

d_{xz}(Pd)
0.95 (Pd), 0.02 (Sn)

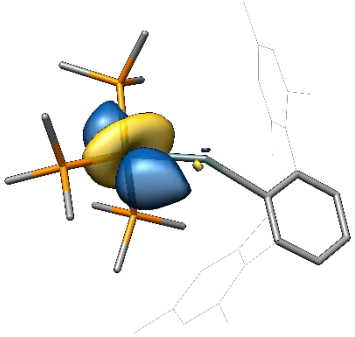

d_{yz}(Pd)
0.88 (Pd), 0.08 (Sn)

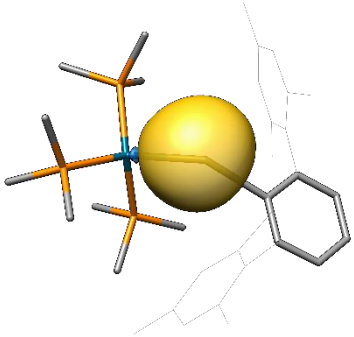

LP(Sn)
0.10 (Pd), 0.91 (Sn)

Figure S33. Selected Pipek-Mezey MOs of compound **PdSnAr^{Mes}**.

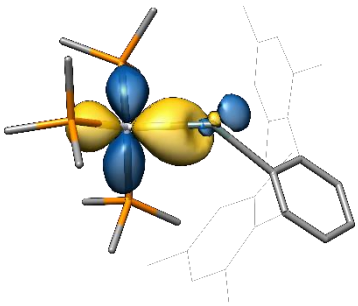

σ(Pt–Sn)
0.81 (Pt), 0.14 (Sn)

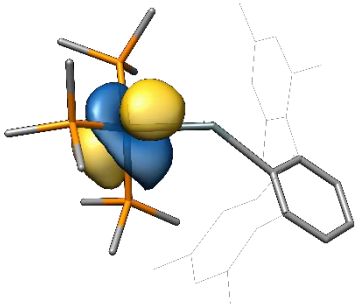

d_{xz}(Pt)
0.94 (Pt), 0.02 (Sn)

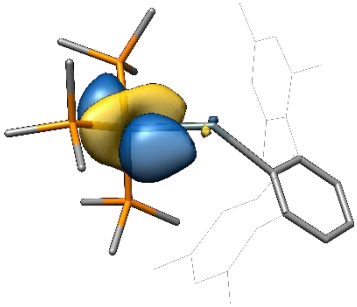

d_{yz}(Pt)
0.87 (Pt), 0.08 (Sn)

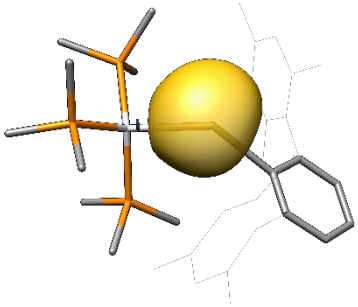

LP(Sn)
0.06 (Pt), 0.97 (Sn)

Figure S34. Selected Pipek-Mezey MOs of compound **PtSnAr^{Mes}**.

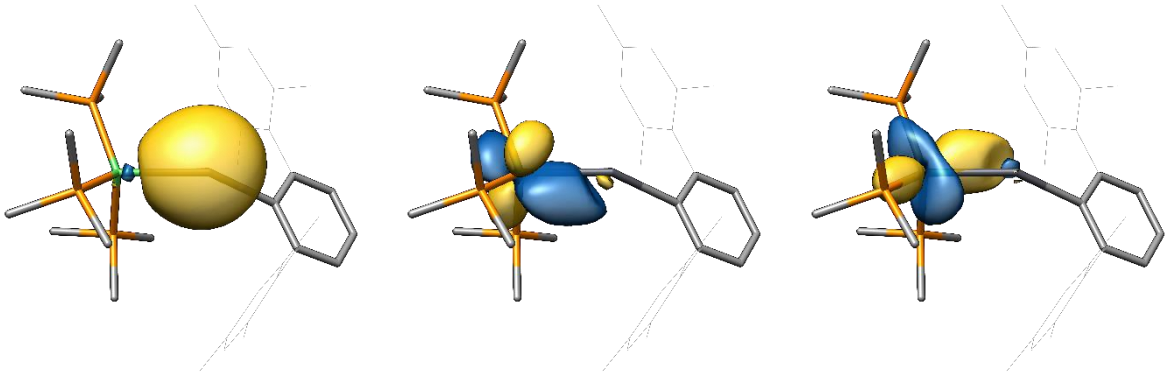

σ(Ni–Pb)
0.07 (Ni), 0.90 (Pb)

π_{xz}(Ni–Pb)
0.85 (Ni), 0.10 (Pb)

π_{yz}(Ni–Pb)
0.84 (Ni), 0.11 (Pb)

Figure S35. Selected Pipek-Mezey MOs of compound **NiPbAr^{Mes}**.

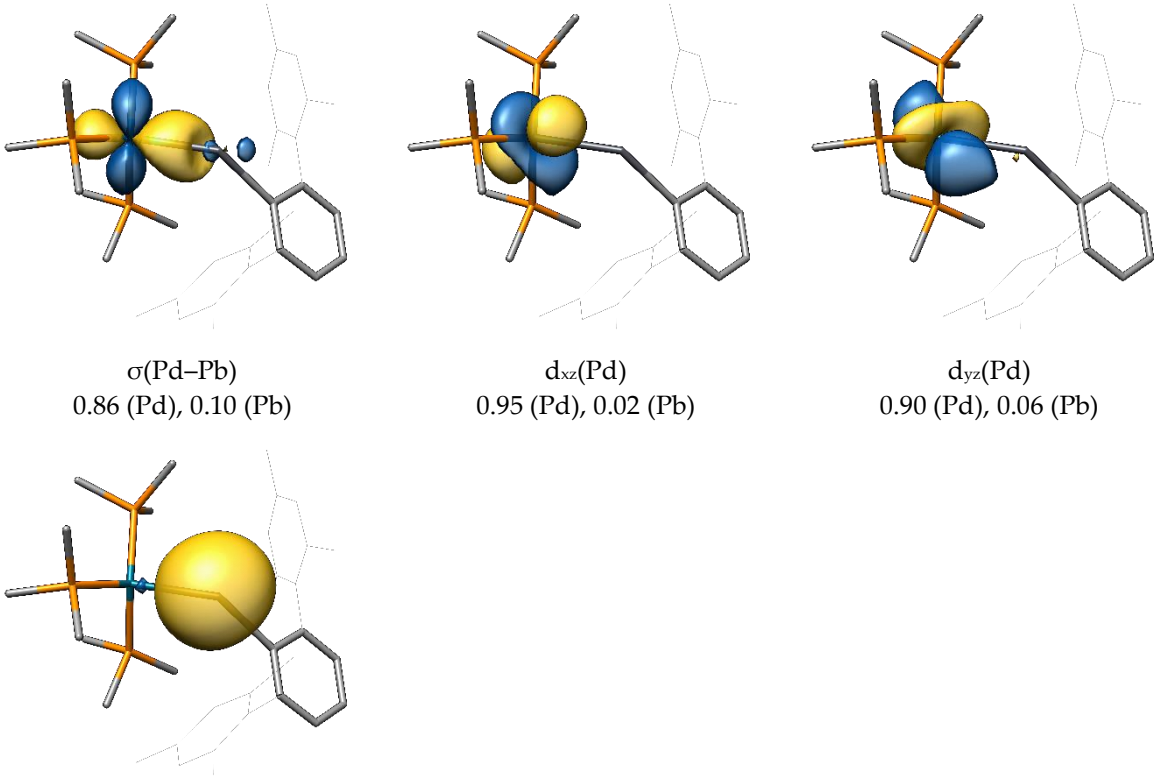

σ(Pd–Pb)
0.86 (Pd), 0.10 (Pb)

d_{xz}(Pd)
0.95 (Pd), 0.02 (Pb)

d_{yz}(Pd)
0.90 (Pd), 0.06 (Pb)

LP(Pb)
0.05 (Pd), 0.93 (Pb)

Figure S36. Selected Pipek-Mezey MOs of compound **PdPbAr^{Mes}**.

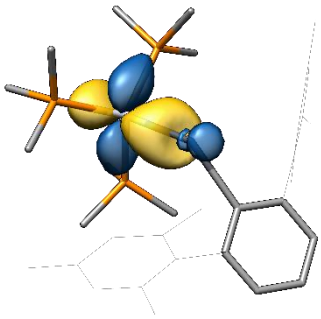

σ(Pt–Pb)
0.82 (Pt), 0.13 (Pb)

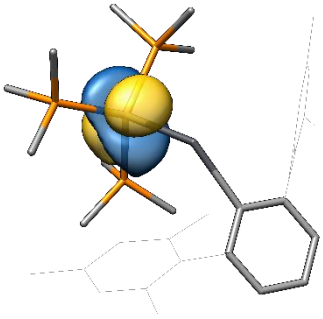

d_{xz}(Pt)
0.95 (Pt), 0.01 (Pb)

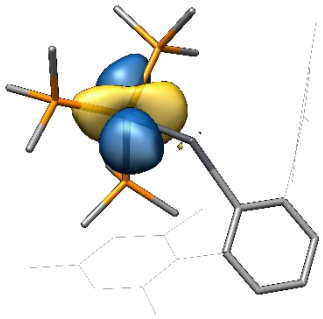

d_{yz}(Pt)
0.89 (Pt), 0.06 (Pb)

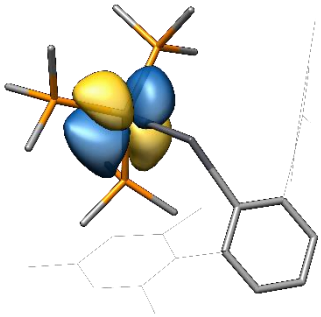

d_{xy}
0.92 (Pt), 0.00 (Pb)

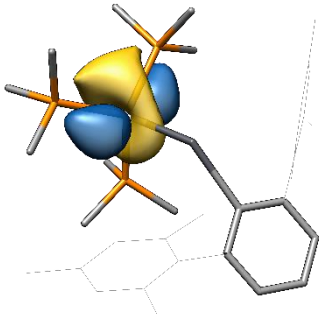

$d_{x^2-y^2}$
0.92 (Pt), 0.00 (Pb)

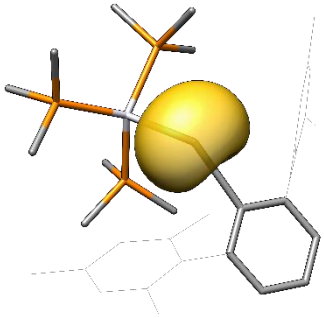

LP(Pb)
0.02 (Pt), 0.96 (Pb)

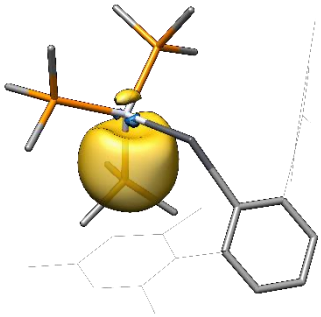

σ(Pt–P1)
0.83 (P1), 0.14 (Pt)

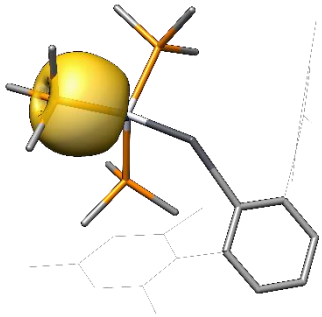

σ(Pt–P2)
0.90 (P2), 0.10 (Pt)

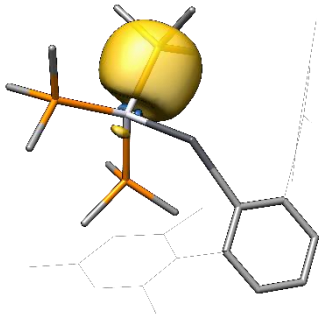

σ(Pt–P3)
0.87 (P3), 0.14 (Pt)

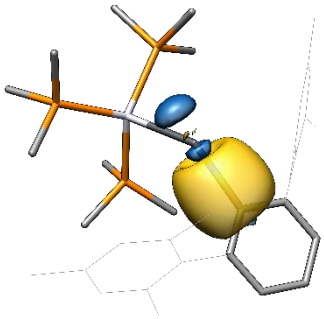

σ(Pb–C1)
0.23 (Pb), 0.85 (C1)

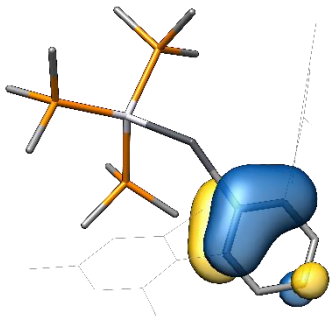

π(C1–C_o–C_o′)
0.02 (Pb), 0.49 (C1),
0.21 (C_o), 0.21 (C_o′)

Figure S37. Selected Pipek-Mezey MOs of compound **PtPbAr^{Mes}**.

7) Selected canonical and localized MOs of compounds **B-Ge** and **B-Sn**

In the main text, some canonical orbitals of **B-Ge** are already presented (**Figure 7**) and show the bonding (π_{xz}), non-bonding ($\pi^{nb}{}_{xz}$) and antibonding ($\pi^{*}{}_{xz}$) combinations of the filled metal d_{xz}, empty tetrel p_x and filled nitrogen p_x orbitals. We searched for the same combinations in the MOs of **B-Sn**, but we were only able to find convincing representations of the $\pi^{nb}{}_{xz}$ and $\pi^{*}{}_{xz}$ orbitals (**Figure S38**), with the π_{xz} combination presumably lying very low in energy and further obscured by the enhanced delocalization caused by the PPh_3 ligands.

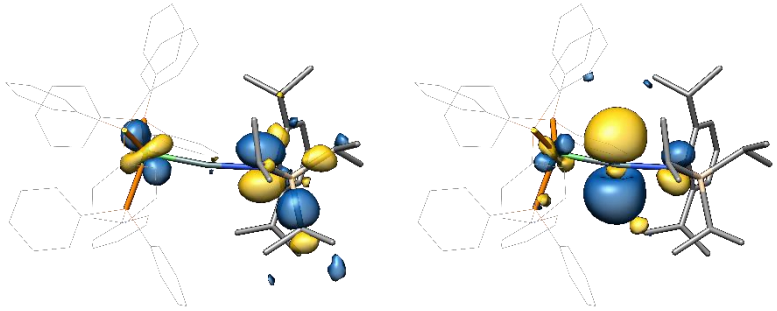

HOMO−3 [−7.51 eV] ($\pi^{nb}{}_{xz}$) LUMO+1 [−4.88 eV] ($\pi^{*}{}_{xz}$)

Figure S38. Selected canonical orbitals of **B-Sn**, their respective orbital energies and the type of bond they represent. Hydrogen atoms are omitted for clarity, the isosurface value is set to 0.04 $e^{1/2}$ $Bohr^{-3/2}$. It was not possible to find a convincing orbital combination of the π_{xz} (all-in-phase) bond, although it is assumed to be present by symmetry considerations of the HOMO−3 and LUMO+1.

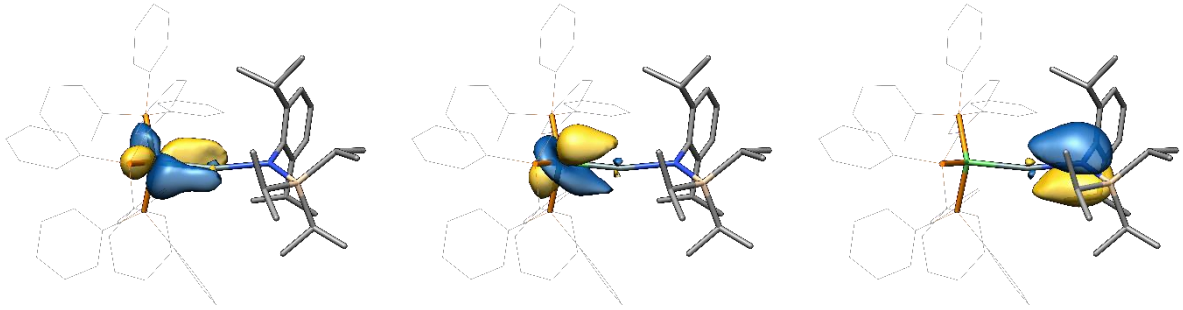

π_{yz}(Ni–Sn)
0.81 (Ni), 0.14 (Sn)

π_{xz}(Ni–Sn)
0.86 (Ni), 0.10 (Sn)

π_{xz}(Sn–N)
0.13 (Sn), 0.83 (N)

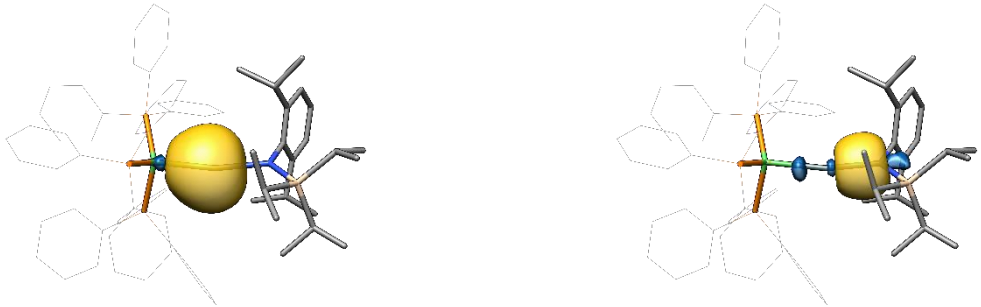

σ(Ni–Sn)
0.18 (Ni), 0.78 (Sn)

σ(Sn–N)
0.35 (Sn), 0.62 (N)

Figure S39. Selected Pipek-Mezey localized molecular orbitals of **B-Sn**, their attributed bond type and corresponding Mulliken populations. Hydrogen atoms are omitted for clarity, the isosurface value is set to 0.04 $e^{1/2}$ $Bohr^{-3/2}$.

However, as for **B-Ge**, the Pipek-Mezey localized MOs reveal the presence of competing π_{xz}(Ni–Sn) and π_{xz}(Sn–N) bonds (**Figure S39**). Based on the associated Mulliken Populations, the LMOs of **B-Sn** can clearly confirm the picture of a tetrylidyne complex with one σ(Sn→M) and two π(M→Sn) dative bonds, whose M≡E bond order is slightly decreased by the competitive π(N→Sn) donation.

As mentioned in the main text, we think that the π_{xz}(M–E) and π_{yz}(M–E) interactions in the canonical HOMO and HOMO−1 are non-bonding interactions. With the same isosurface value as for our own complexes in this study (0.04 $e^{1/2}$ $Bohr^{-3/2}$), the HOMO−1 of **B-Ge** is mostly metal-centred (**Figure S40 a**), but when the isosurface value is decreased to 0.02 $e^{1/2}$ $Bohr^{-3/2}$, it shows a considerable orbital lobe on the germanium atom, which can be easily misunderstood as bonding interaction. However, by closer inspection of the lobes and comparison with our own complexes (see **Figure S40 c** and also section 5 of the SI), only half of the metal d-orbital can positively interact with the tetrel p-orbital, whereas the other half has a negative interaction being anti-bonding. In total, this leads to a cancellation of both interactions, being non-bonding in total.

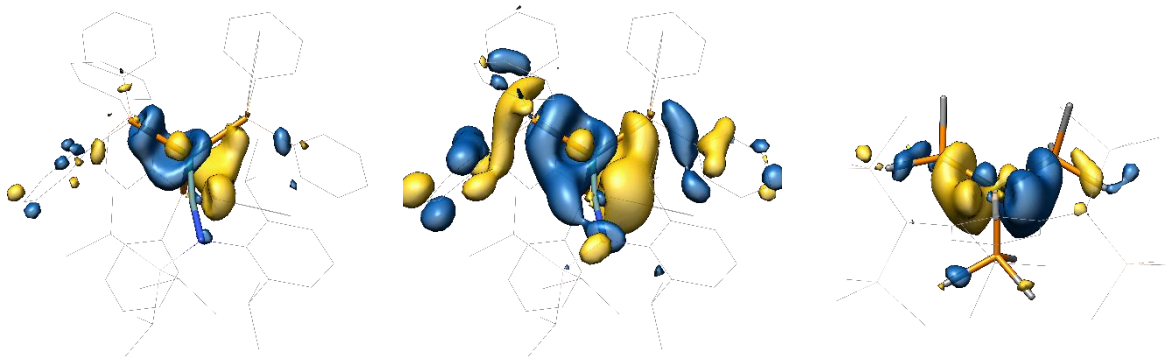

a) HOMO−1 of **B-Ge** (0.04 $e^{1/2}$ $Bohr^{-3/2}$) | b) HOMO−1 of **B-Ge** (0.02 $e^{1/2}$ $Bohr^{-3/2}$) | c) HOMO−1 of **NiSiTbb** (0.04 $e^{1/2}$ $Bohr^{-3/2}$)

Figure S40. Canonical HOMO−1 of **B-Ge** (a,b) and **NiSiTbb** (c) for comparison with different isosurface values in brackets. The view for a) and b) is slightly above the Ge–Ni bond axis, while for c) it is along the Si–Ni bond axis to highlight the non-bonding nature of this MO. Hydrogen atoms are omitted for clarity.

8) Spin-spin excitation energies for the fragments of compounds **MER**

Table S6. Electronic singlet-triplet ΔE_{el}(s→t) and doublet–quartet ΔE_{el}(d→q) excitation energies for the structurally relaxed fragments of **MER** in $kJ \cdot mol^{-1}$.

	Level of theory I		Level of theory II	
fragment	**ΔE_{el}(s→t)**	**ΔE_{el}(d→q)**	**ΔE_{el}(s→t)**	**ΔE_{el}(d→q)**
$[Ni(PMe_3)_3]^{0/+}$	191.4	232.5	209.3	241.8
$[Pd(PMe_3)_3]^{0/+}$	214.3	284.0	218.4	297.7
$[Pt(PMe_3)_3]^{0/+}$	195.3	260.5	198.9	269.0
$CArMes^{+/0}$	−31.6	120.3	−33.2	137.6
$SiTbb^{+/0}$	140.8	175.6	170.1	200.8
$SiAr^{Mes+/0}$	158.9	191.9	191.1	216.8
$GeAr^{Mes+/0}$	164.8	209.2	-[a]	230.0
$SnAr^{Mes+/0}$	174.7	212.1	-[a]	228.1
$PbAr^{Mes+/0}$	173.2	218.7	197.7	233.8

a) No SCF convergence could be achieved for the triplet state.

9) *BCEs* and *BDEs* of **MSiAr^{Mes}**

Table S7. Calculated *BCE*s and *BDE*s in kJ·mol^{-1} on the level of theory **II** of the M–E bonds of the [L$_3$MER]$^+$ complexes leading to the ML$_3$ + ER$^+$ and ML$_3^+$ + ER fragment combinations. *BCE*s and *BDE*s of the energetically favourable fragmentation scheme are highlighted bold.

	BCE		*BDE*	
compound	**ML$_3$ + ER$^+$**	**ML$_3^+$ + ER**	**ML$_3$ + ER$^+$**	**ML$_3^+$ + ER**
NiSiAr^{Mes}	491.5	**421.4**	392.3	**368.9**
PdSiAr^{Mes}	427.4	**387.9**	322.5	**295.3**
PtSiAr^{Mes}	520.3	**450.2**	362.1	**324.1**

10) Thermodynamically corrected *BDE*s

The given thermodynamic parameters are defined as follows:

a. E_{el} – The electronic energy is defined as the sum of the components of the single point energy, resulting from the application of the Hamiltonian H to the N-electron wavefunction Ψ. This consists of the kinetic energy T, attraction between the nuclei and electrons E_{ne}, the electron-electron repulsion E_{ee}, the nuclear repulsion E_{nn} and other correcting terms like Grimme's correction for London dispersion forces E_{disp} and its three-body correction E_{ATM}:

$$H\Psi = E_{el}\Psi = (T + E_{ne} + E_{ee} + E_{nn} + E_{disp} + E_{ATM})\Psi.$$

b. *BCE* – The bond cleavage energy is defined as the difference of the electronic energies E_{el} of two structurally unrelaxed fragments (A and B) and the unfragmented compound (AB). Herein the total spin of the two fragments must be equal to the spin of the molecule AB:

$$BCE = E_{el}(A) + E_{el}(B) - E_{el}(AB).$$

c. ΔE_{relax} – The structural relaxation energy is the energy difference between the electronic energies of the structurally unrelaxed (X) and relaxed fragment (X*):

$$\Delta E_{relax}(X) = E_{el}(X) - E_{el}(X^*).$$

d. *BDE* – The bond dissociation energy is the difference between the *BCE* and structural relaxation energies of the fragments:

$$BDE = BCE - \Delta E_{relax}(A) - \Delta E_{relax}(B).$$

e. U(0 K) – The inner energy at 0 K is the sum of the electronic energy and the zero point vibrational energy E_{ZPVE}:

$$U(0\ \mathrm{K}) = E_{el} + E_{ZPVE}.$$

f. $U°$ – The inner energy at standard ambient conditions (T = 298.15 K, p = 100.000 kPa) additionally takes the temperature dependent vibrational (E_{vib}), rotational (E_{rot}) and translational (E_{trans}) terms into account:

$$U° = E_{el} + E_{ZPVE} + E_{vib} + E_{rot} + E_{trans}.$$

g. $H°$ – The enthalpy at standard ambient conditions is then given as:

$$H° = U° + k_B T.$$

h. $S°$ – The entropy is made up of electronic (S_{el}), vibrational (S_{vib}), rotational (S_{rot}) and translational (S_{trans}) contributions:

$$S° = S_{el} + S_{vib} + S_{rot} + S_{trans}.$$

i. $G°$ – The Gibbs free energy is given as:

$$G = H - TS.$$

Table S8. Energies in kJ·mol^{-1} for the dissociation of the M–E bonds of the [L$_3$MER]$^+$ complexes into the ML$_3$ + ER$^+$ fragments obtained on the level of theory **II**. Entropies are given in J·mol^{-1}·K^{-1}. Thermodynamic corrections to the electronic energies are calculated on the level of theory **I**.

compound	*BCE*	ΔE_{relax}(ML$_3$)	ΔE_{relax}(ER$^+$)	*BDE*	ΔU(0 K)	$\Delta U°$	$\Delta H°$	$\Delta S°$	$\Delta G°$
NiCArMes	718.6	104.0	92.8	521.8	507.5	504.3	506.8	238.5	435.7
NiSiTbb	470.4	52.7	15.2	402.5	383.3	383.1	385.5	263.3	307.0
NiSiArMes	491.5	54.7	44.5	392.3	381.6	381.0	383.4	246.5	310.0
NiGeArMes	459.3	52.7	41.6	365.0	354.1	351.2	353.7	229.6	285.2
NiSnArMes	383.9	36.7	30.4	316.9	306.4	303.4	305.8	233.6	236.2
NiPbArMes	342.7	27.9	23.0	291.7	281.7	278.4	280.9	235.6	210.7
PdCArMes	625.1	133.6	87.3	404.2	391.9	386.0	388.5	221.2	322.6
PdSiTbb	415.3	69.1	13.2	333.0	316.9	315.4	317.9	255.5	241.7
PdSiArMes	427.4	65.4	39.5	322.5	312.6	309.6	312.1	234.9	242.1
PdGeArMes	383.2	54.3	39.5	289.4	278.8	276.5	278.9	244.4	206.1
PdSnArMes	321.9	34.6	33.7	253.6	242.7	240.4	242.9	247.1	169.2
PdPbArMes	293.3	26.3	26.6	240.4	229.8	227.2	229.6	243.7	157.0
PtCArMes	799.3	224.3	89.0	486.0	471.9	466.5	468.9	225.6	401.7
PtSiTbb	504.0	116.9	13.5	373.5	357.1	355.3	357.8	251.4	282.8
PtSiArMes	520.3	117.6	40.6	362.1	351.9	348.7	351.2	224.8	284.2
PtGeArMes	444.0	89.6	39.8	314.5	303.0	301.0	303.5	248.0	229.5
PtSnArMes	354.6	44.0	36.5	274.1	263.5	260.9	263.4	242.7	191.0
PtPbArMes	313.5	33.9	28.5	251.1	238.7	237.1	239.6	256.1	163.2

Table S9. Energies in kJ·mol^{-1} for the dissociation of the M–E bonds of the $[L_3MER]^+$ complexes into the ML_3^+ + ER fragments obtained on the level of theory **II**. Entropies are given in J·mol^{-1}·K^{-1}. Thermodynamic corrections to the electronic energies are calculated on level of theory **I**.

compound	*BCE*	$\Delta E_{relax}(ML_3^+)$	ΔE_{relax}(ER)	*BDE*	ΔU(0 K)	$\Delta U°$	$\Delta H°$	$\Delta S°$	$\Delta G°$
NiCAr^{Mes}	544.3	69.7	12.9	461.6	442.1	443.9	446.3	283.5	361.8
NiSiTbb	427.9	42.8	7.5	377.5	364.2	363.7	366.2	269.1	286.0
NiSiAr^{Mes}	421.4	42.0	10.4	368.9	359.2	360.0	362.5	269.2	282.2
NiGeAr^{Mes}	387.7	40.4	7.3	340.0	330.0	328.7	331.1	255.6	254.9
NiSnAr^{Mes}	346.0	33.7	7.9	304.5	295.7	294.1	296.6	256.2	220.1
NiPbAr^{Mes}	328.6	32.0	11.0	285.6	279.0	276.0	278.4	246.5	204.9
PdCAr^{Mes}	469.7	122.0	7.5	340.1	323.8	321.7	324.2	251.4	249.2
PdSiTbb	395.0	84.1	6.8	304.1	295.0	292.2	294.7	246.5	221.2
PdSiAr^{Mes}	387.9	79.7	12.9	295.3	287.4	284.8	287.2	242.9	214.8
PdGeAr^{Mes}	349.2	73.5	15.2	260.5	251.9	250.1	252.5	255.7	176.3
PdSnAr^{Mes}	319.5	64.0	18.1	237.3	229.3	227.3	229.8	255.0	153.8
PdPbAr^{Mes}	309.0	59.3	19.3	230.4	224.3	220.8	223.3	239.8	151.8
PtCAr^{Mes}	618.3	200.3	6.8	411.3	393.2	391.6	394.1	259.0	316.9
PtSiTbb	462.5	123.8	4.7	334.0	324.6	321.6	324.1	245.7	250.8
PtSiAr^{Mes}	450.2	119.4	6.6	324.1	316.1	313.4	315.9	236.0	245.5
PtGeAr^{Mes}	386.3	99.9	11.5	274.9	265.5	264.1	266.5	262.5	188.3
PtSnAr^{Mes}	332.6	66.0	19.4	247.2	239.4	237.3	239.7	253.8	164.1
PtPbAr^{Mes}	307.8	57.4	19.9	230.5	222.6	220.2	222.7	255.4	146.5

11) EDA components of the interaction energy of **MER**

Table S10. Detailed results of the EDA of the **MER** compounds. Energies are given in kJ·mol^{-1}.

compound	ΔE_{orb}	ΔE_{Pauli}	ΔE_{elstat}	ΔE_{disp}	ΔE_{int}
NiCAr^{Mes}	−645.3	1076.6	−820.6	−138.3	−527.5
NiSiTbb	−498.1	699.7	−528.8	−131.0	−458.2
NiSiAr^{Mes}	−486.2	815.4	−591.5	−131.4	−393.6
NiGeAr^{Mes}	−443.5	683.7	−482.6	−120.8	−363.3
NiSnAr^{Mes}	−372.7	521.9	−399.7	−117.7	−368.2
NiPbAr^{Mes}	−331.9	495.9	−368.8	−126.1	−330.9
PdCAr^{Mes}	−671.7	1244.0	−915.6	−126.1	−469.7
PdSiTbb	−472.0	857.3	−674.5	−116.3	−405.5
PdSiAr^{Mes}	−494.5	999.6	−755.8	−127.0	−377.7
PdGeAr^{Mes}	−426.8	688.9	−515.6	−125.1	−378.5
PdSnAr^{Mes}	−334.8	566.5	−430.7	−124.4	−312.5
PdPbAr^{Mes}	−291.1	499.0	−371.0	−130.4	−293.5
PtCAr^{Mes}	−903.3	1674.8	−1247.3	−132.1	−607.8
PtSiTbb	−585.8	1077.6	−863.1	−118.9	−490.3
PtSiAr^{Mes}	−573.8	1192.5	−929.4	−124.8	−435.5
PtGeAr^{Mes}	−499.1	1009.9	−762.2	−124.6	−376.0
PtSnAr^{Mes}	−380.4	668.3	−507.0	−132.5	−351.6
PtPbAr^{Mes}	−319.6	559.1	−417.7	−136.7	−314.9

12) ETS-NOCV deformation densities of compounds **MER**

Isosurface plots (isosurface value = 0.002 e Bohr^{-3}) of deformation densities ($\Delta\rho_n$) in e Bohr^{-3} of complementary NOCVs (ψ_{-n} and ψ_{+n}), split into α- and β-spin derived deformation densities when required, given with their respective eigenvalues (ν_{-n} and ν_{+n}). Regions of charge depletion ($\Delta\rho_n < 0$ e Bohr^{-3}) are shown in red and regions of charge accumulation ($\Delta\rho_n > 0$ e Bohr^{-3}) in grey. Level of theory: B97-D3(BJ)/TZ2P//**I**.

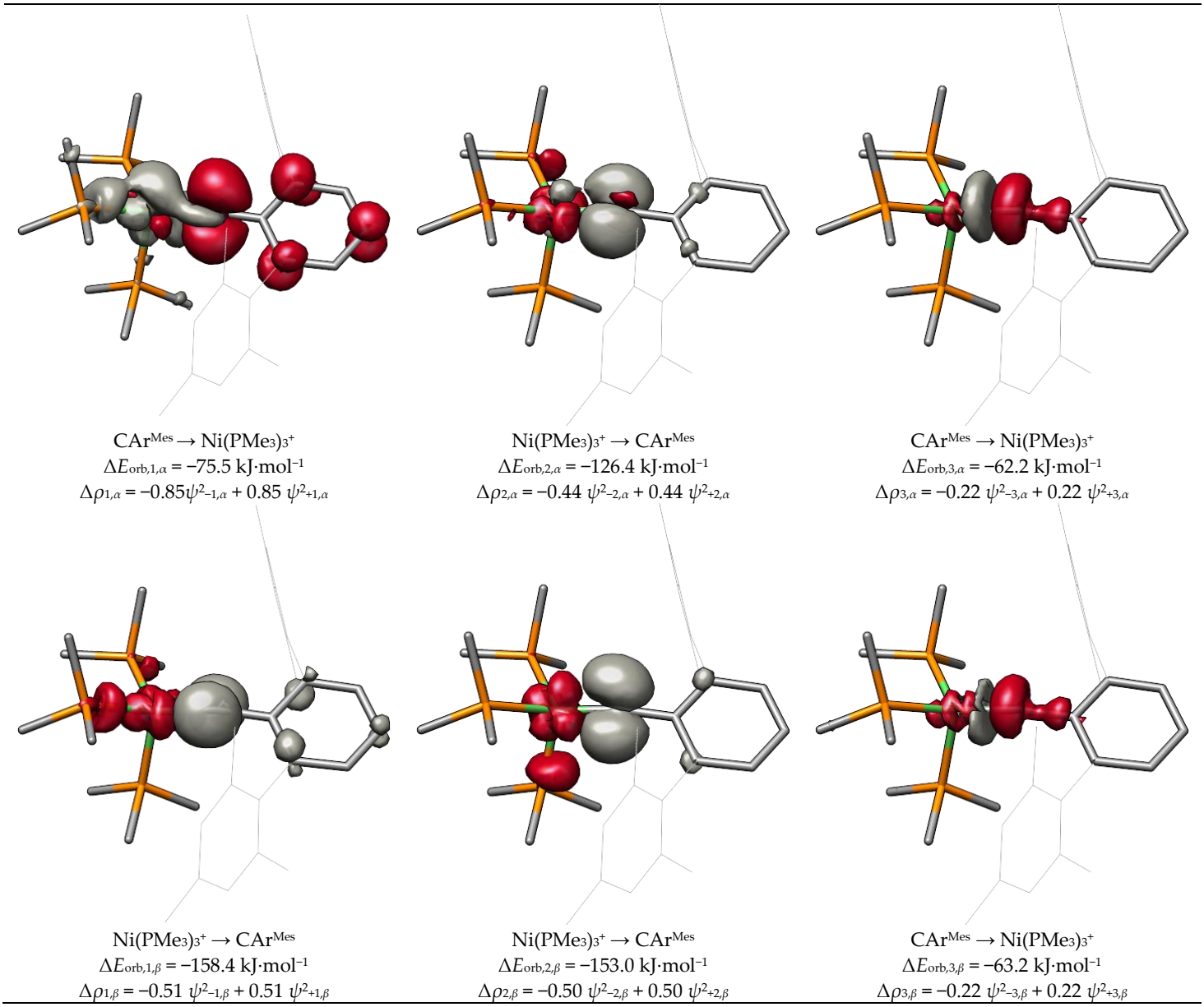

Figure S41. Deformation densities of **NiCAr^{Mes}**.

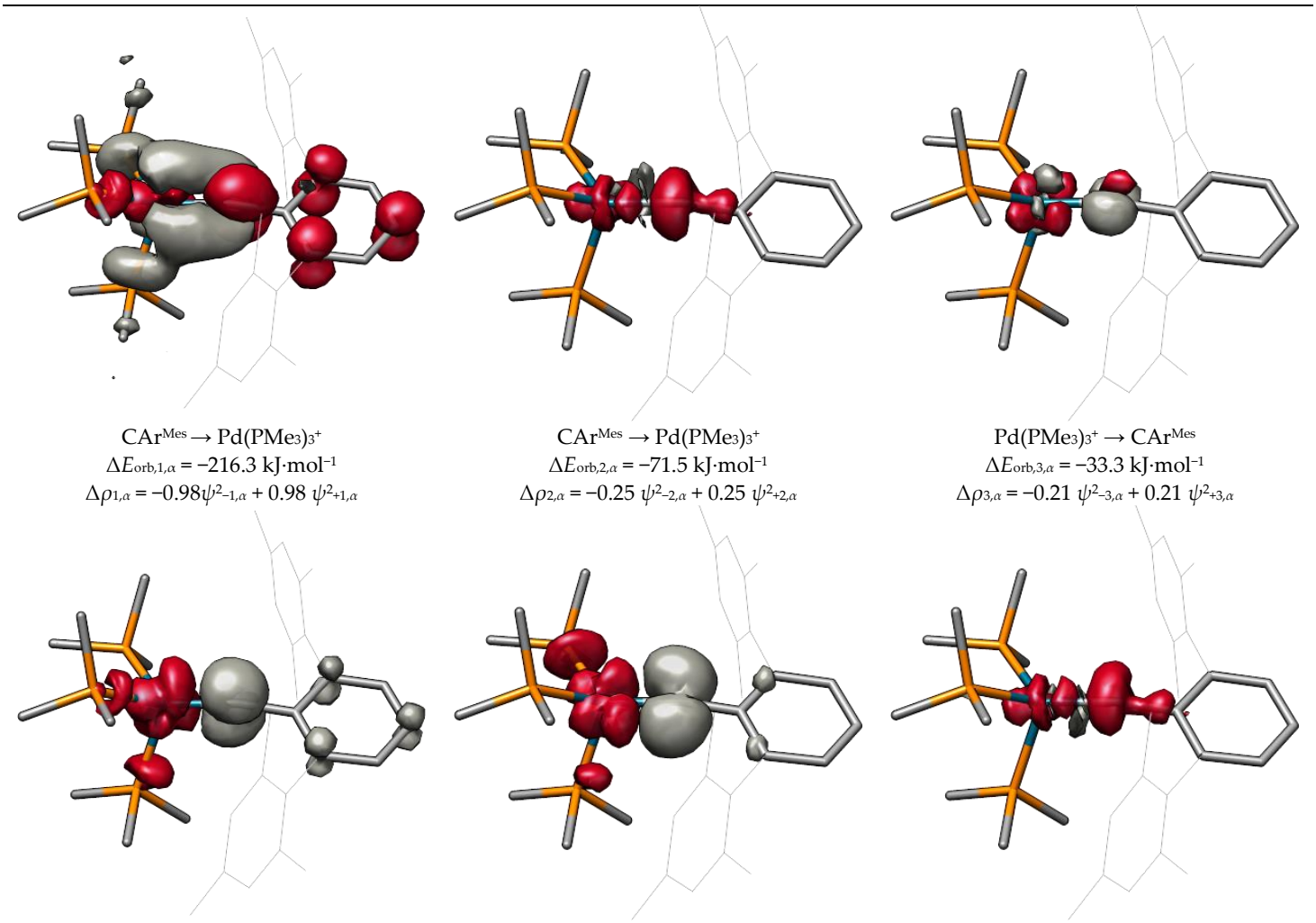

Figure S42. Deformation densities of **PdCAr^{Mes}**.

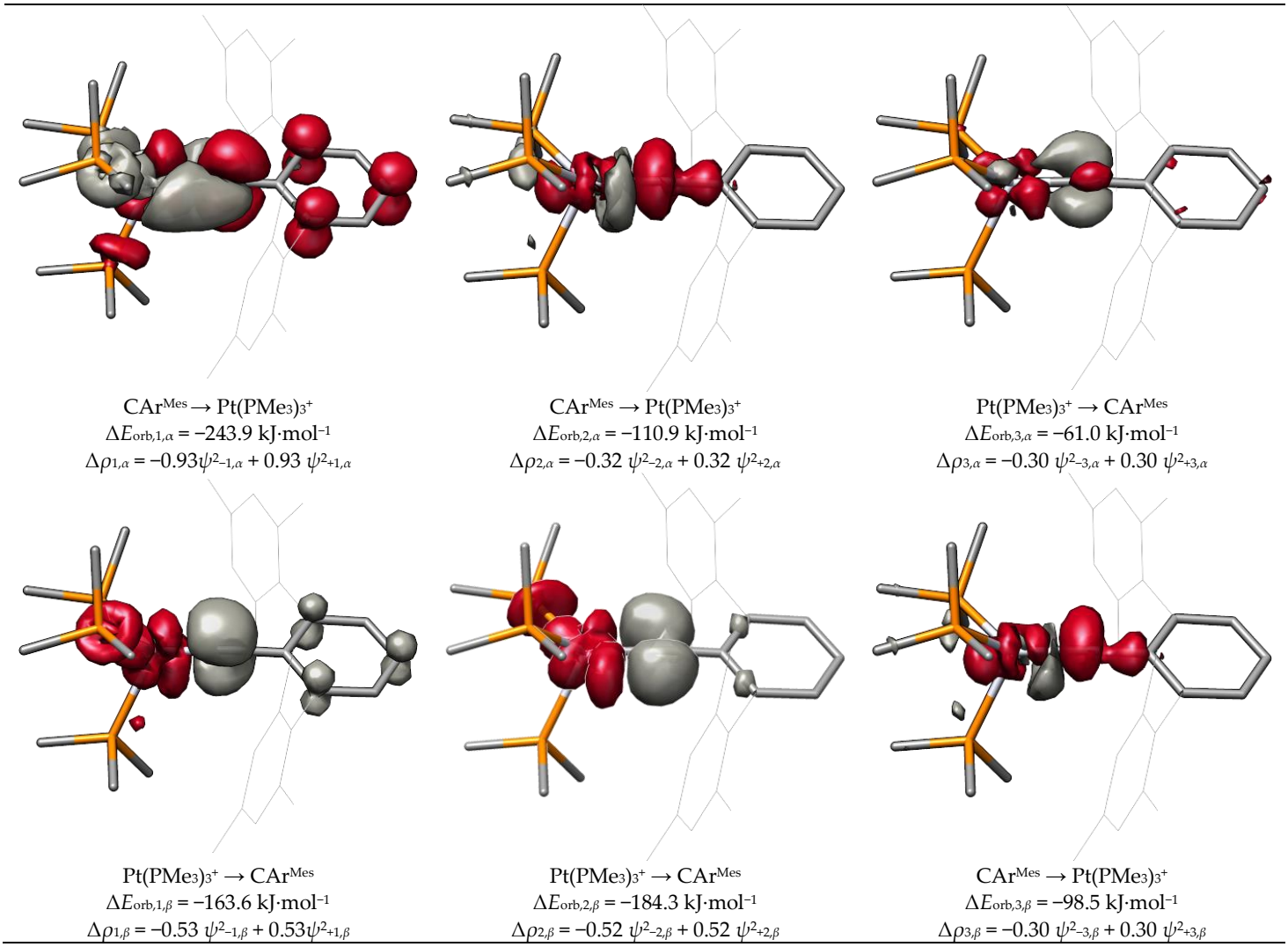

$CAr^{Mes} \rightarrow Pt(PMe_3)_3^+$
$\Delta E_{orb,1,\alpha} = -243.9$ kJ·mol^{-1}
$\Delta\rho_{1,\alpha} = -0.93\psi^2_{-1,\alpha} + 0.93\ \psi^2_{+1,\alpha}$

$CAr^{Mes} \rightarrow Pt(PMe_3)_3^+$
$\Delta E_{orb,2,\alpha} = -110.9$ kJ·mol^{-1}
$\Delta\rho_{2,\alpha} = -0.32\ \psi^2_{-2,\alpha} + 0.32\ \psi^2_{+2,\alpha}$

$Pt(PMe_3)_3^+ \rightarrow CAr^{Mes}$
$\Delta E_{orb,3,\alpha} = -61.0$ kJ·mol^{-1}
$\Delta\rho_{3,\alpha} = -0.30\ \psi^2_{-3,\alpha} + 0.30\ \psi^2_{+3,\alpha}$

$Pt(PMe_3)_3^+ \rightarrow CAr^{Mes}$
$\Delta E_{orb,1,\beta} = -163.6$ kJ·mol^{-1}
$\Delta\rho_{1,\beta} = -0.53\ \psi^2_{-1,\beta} + 0.53\psi^2_{+1,\beta}$

$Pt(PMe_3)_3^+ \rightarrow CAr^{Mes}$
$\Delta E_{orb,2,\beta} = -184.3$ kJ·mol^{-1}
$\Delta\rho_{2,\beta} = -0.52\ \psi^2_{-2,\beta} + 0.52\ \psi^2_{+2,\beta}$

$CAr^{Mes} \rightarrow Pt(PMe_3)_3^+$
$\Delta E_{orb,3,\beta} = -98.5$ kJ·mol^{-1}
$\Delta\rho_{3,\beta} = -0.30\ \psi^2_{-3,\beta} + 0.30\ \psi^2_{+3,\beta}$

Figure S43. Deformation densities of **PtCAr^{Mes}**.

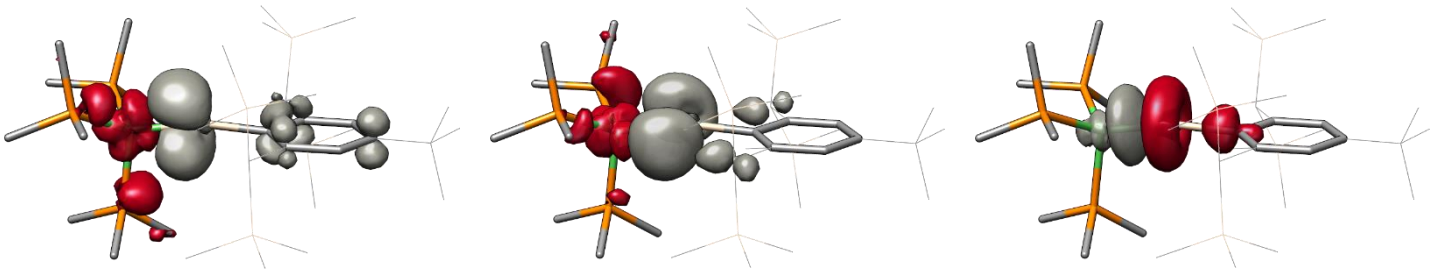

HOMO−1(Ni(PMe$_3$)$_3$)→LUMO+1(SiTbb$^+$)
$\Delta E_{orb,1} = -199.6$ kJ·mol^{-1}
$\Delta\rho_1 = -0.77\ \psi^2_{-1} + 0.77\ \psi^2_{+1}$

HOMO(Ni(PMe$_3$)$_3$)→LUMO(SiTbb$^+$)
$\Delta E_{orb,2} = -206.8$ kJ·mol^{-1}
$\Delta\rho_2 = -0.76\ \psi^2_{-2} + 0.76\ \psi^2_{+2}$

HOMO−10(SiTbb$^+$)→LUMO(Ni(PMe$_3$)$_3$)
$\Delta E_{orb,3} = -53.5$ kJ·mol^{-1}
$\Delta\rho_3 = -0.39\ \psi^2_{-3} + 0.39\ \psi^2_{+3}$

Figure S44. Deformation densities of **NiSiTbb**.

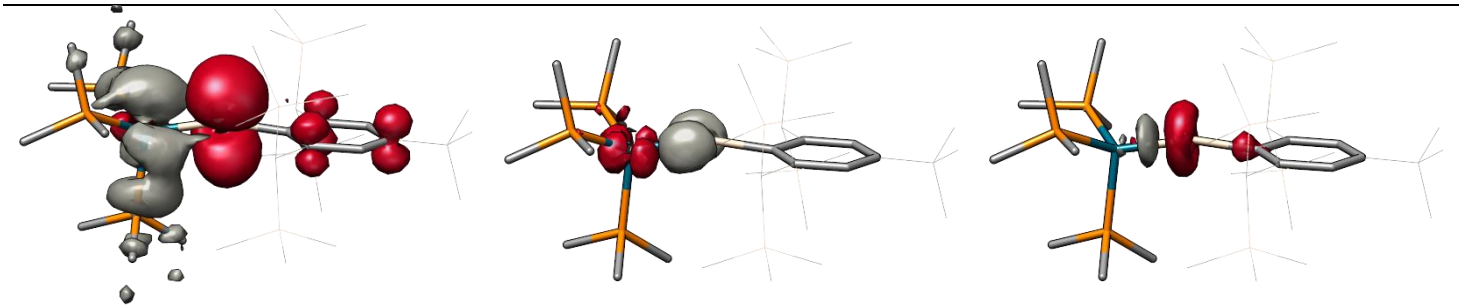

SiTbb → $Pd(PMe_3)_3^+$
$\Delta E_{orb,1,\alpha} = -171.7$ kJ·mol^{-1}
$\Delta\rho_{1,\alpha} = -0.91\psi^2_{-1,\alpha} + 0.91\ \psi^2_{+1,\alpha}$

$Pd(PMe_3)_3^+$ → SiTbb
$\Delta E_{orb,2,\alpha} = -56.1$ kJ·mol^{-1}
$\Delta\rho_{2,\alpha} = -0.30\ \psi^2_{-2,\alpha} + 0.30\ \psi^2_{+2,\alpha}$

SiTbb → $Pd(PMe_3)_3^+$
$\Delta E_{orb,3,\alpha} = -31.8$ kJ·mol^{-1}
$\Delta\rho_{3,\alpha} = -0.18\ \psi^2_{-3,\alpha} + 0.18\ \psi^2_{+3,\alpha}$

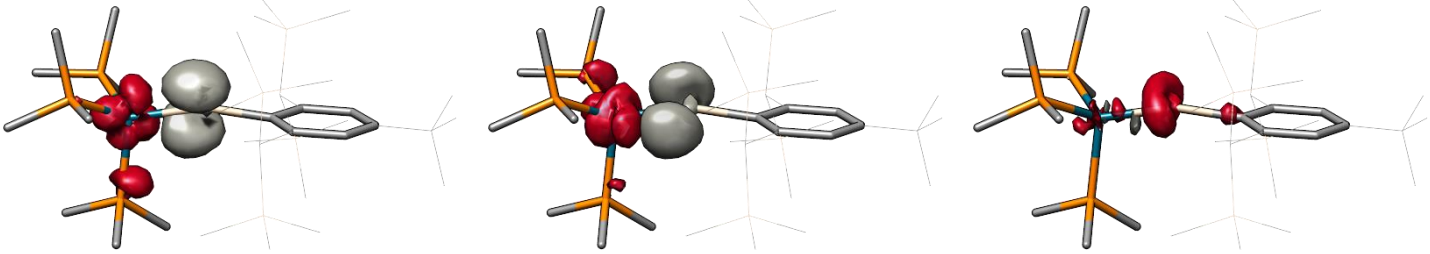

$Pd(PMe_3)_3^+$ → SiTbb
$\Delta E_{orb,1,\beta} = -65.2$ kJ·mol^{-1}
$\Delta\rho_{1,\beta} = -0.36\ \psi^2_{-1,\beta} + 0.36\psi^2_{+1,\beta}$

$Pd(PMe_3)_3^+$ → SiTbb
$\Delta E_{orb,2,\beta} = -69.9$ kJ·mol^{-1}
$\Delta\rho_{2,\beta} = -0.35\ \psi^2_{-2,\beta} + 0.35\ \psi^2_{+2,\beta}$

SiTbb → $Pd(PMe_3)_3^+$
$\Delta E_{orb,3,\beta} = -31.9$ kJ·mol^{-1}
$\Delta\rho_{3,\beta} = -0.17\ \psi^2_{-3,\beta} + 0.17\ \psi^2_{+3,\beta}$

Figure S45. Deformation densities of **PdSiTbb**.

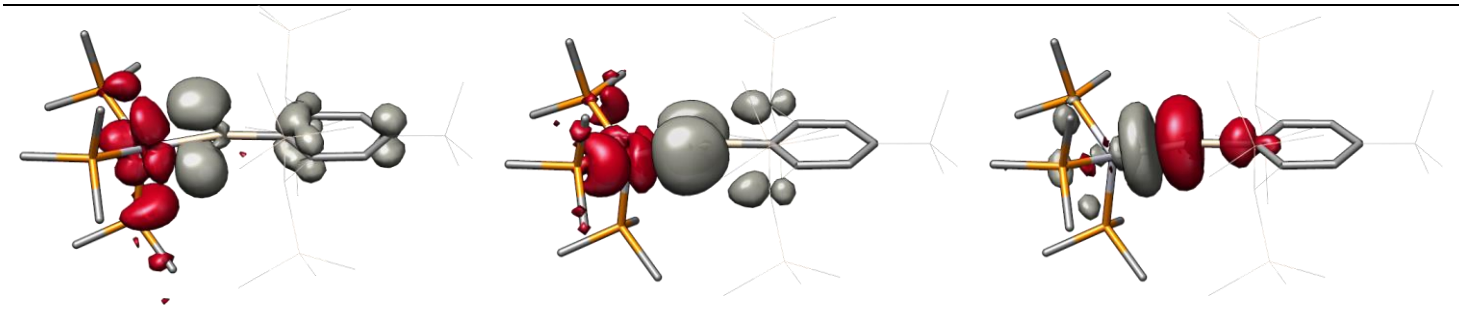

HOMO−1($Pt(PMe_3)_3$)→LUMO+1($SiTbb^+$)
$\Delta E_{orb,1} = -194.7$ kJ·mol^{-1}
$\Delta\rho_1 = -0.78\ \psi^2_{-1} + 0.78\ \psi^2_{+1}$

HOMO($Pt(PMe_3)_3$)→LUMO($SiTbb^+$)
$\Delta E_{orb,2} = -205.5$ kJ·mol^{-1}
$\Delta\rho_2 = -0.77\ \psi^2_{-2} + 0.77\ \psi^2_{+2}$

HOMO−10($SiTbb^+$)→LUMO($Pt(PMe_3)_3$)
$\Delta E_{orb,3} = -82.4$ kJ·mol^{-1}
$\Delta\rho_3 = -0.47\ \psi^2_{-3} + 0.47\ \psi^2_{+3}$

Figure S46. Deformation densities of **PtSiTbb**.

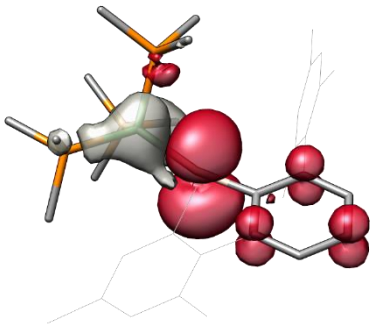

SOMO(SiAr^{Mes})→SOMO(Ni(PMe$_3$)$_3^+$)
$\Delta E_{orb,1,\alpha} = -140.1$ kJ·mol^{-1}
$\Delta\rho_{1,\alpha} = -0.90\ \psi^2_{-1,\alpha} + 0.90\ \psi^2_{+1,\alpha}$

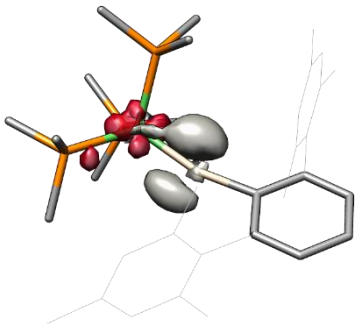

HOMO−3(Ni(PMe$_3$)$_3^+$)→LUMO(SiAr^{Mes})
$\Delta E_{orb,2,\alpha} = -55.1$ kJ·mol^{-1}
$\Delta\rho_{2,\alpha} = -0.29\ \psi^2_{-2,\alpha} + 0.29\ \psi^2_{+2,\alpha}$

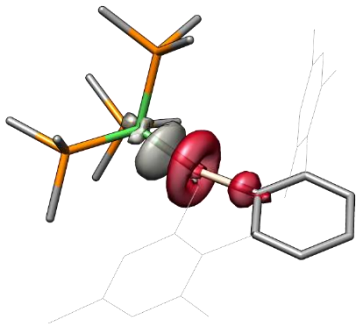

HOMO(SiAr^{Mes})→LUMO(Ni(PMe$_3$)$_3^+$)
$\Delta E_{orb,3,\alpha} = -37.4$ kJ·mol^{-1}
$\Delta\rho_{3,\alpha} = -0.19\ \psi^2_{-3,\alpha} + 0.19\ \psi^2_{+3,\alpha}$

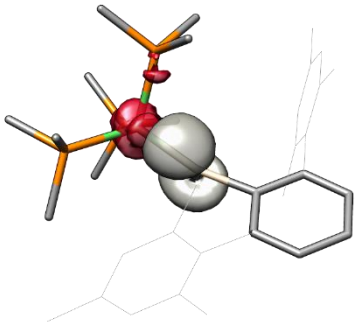

SOMO(Ni(PMe$_3$)$_3^+$)→SOMO(SiAr^{Mes})
$\Delta E_{orb,1,\beta} = -82.7$ kJ·mol^{-1}
$\Delta\rho_{1,\beta} = -0.41\ \psi^2_{-1,\beta} + 0.41\ \psi^2_{+1,\beta}$

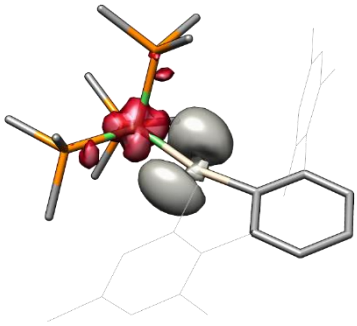

HOMO−3(Ni(PMe$_3$)$_3^+$)→LUMO(SiAr^{Mes})
$\Delta E_{orb,2,\beta} = -84.7$ kJ·mol^{-1}
$\Delta\rho_{2,\beta} = -0.37\ \psi^2_{-2,\beta} + 0.37\ \psi^2_{+2,\beta}$

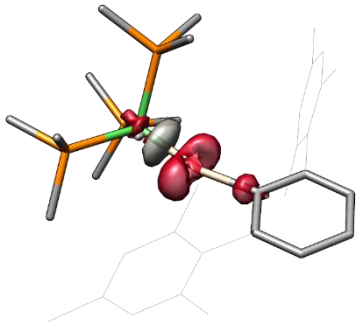

HOMO(SiAr^{Mes})→LUMO(Ni(PMe$_3$)$_3^+$)
$\Delta E_{orb,3,\beta} = -36.5$ kJ·mol^{-1}
$\Delta\rho_{3,\beta} = -0.18\ \psi^2_{-3,\beta} + 0.18\ \psi^2_{+3,\beta}$

Figure S47. Deformation densities of **NiSiAr^{Mes}**.

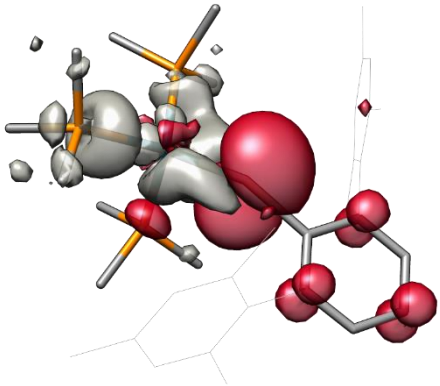

SOMO(SiAr^{Mes})→SOMO(Pd(PMe$_3$)$_3^+$)
$\Delta E_{orb,1,\alpha}$ = −194.7 kJ·mol^{-1}
$\Delta\rho_{1,\alpha}$ = −0.93 $\psi^2_{-1,\alpha}$ + 0.93 $\psi^2_{+1,\alpha}$

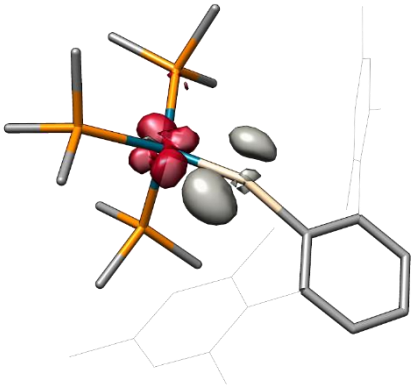

HOMO−3(Pd(PMe$_3$)$_3^+$)→LUMO(SiAr^{Mes})
$\Delta E_{orb,2,\alpha}$ = −37.5 kJ·mol^{-1}
$\Delta\rho_{2,\alpha}$ = −0.23 $\psi^2_{-2,\alpha}$ + 0.23 $\psi^2_{+2,\alpha}$

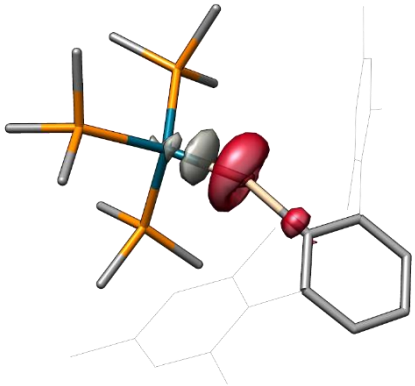

HOMO(SiAr^{Mes})→LUMO(Pd(PMe$_3$)$_3^+$)
$\Delta E_{orb,3,\alpha}$ = −26.6 kJ·mol^{-1}
$\Delta\rho_{3,\alpha}$ = −0.16 $\psi^2_{-3,\alpha}$ + 0.16 $\psi^2_{+3,\alpha}$

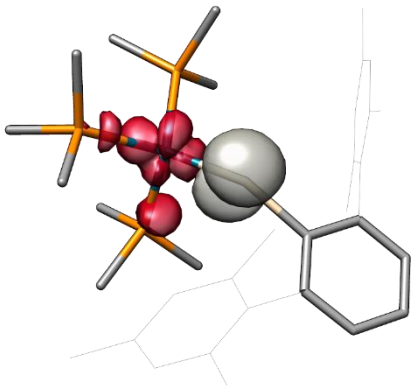

SOMO(Pd(PMe$_3$)$_3^+$)→SOMO(SiAr^{Mes})
$\Delta E_{orb,1,\beta}$ = −78.2 kJ·mol^{-1}
$\Delta\rho_{1,\beta}$ = −0.38 $\psi^2_{-1,\beta}$ + 0.38 $\psi^2_{+1,\beta}$

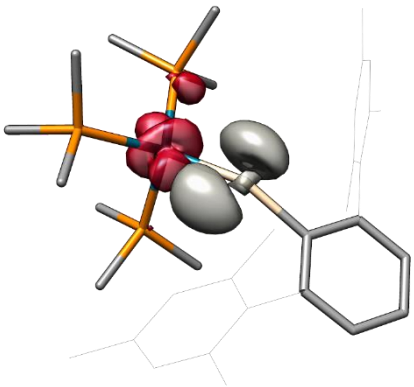

HOMO−3(Pd(PMe$_3$)$_3^+$)→LUMO(SiAr^{Mes})
$\Delta E_{orb,2,\beta}$ = −68.4 kJ·mol^{-1}
$\Delta\rho_{2,\beta}$ = −0.34 $\psi^2_{-2,\beta}$ + 0.34 $\psi^2_{+2,\beta}$

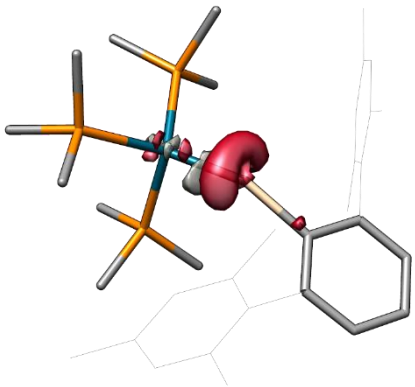

HOMO(SiAr^{Mes})→LUMO(Pd(PMe$_3$)$_3^+$)
$\Delta E_{orb,3,\beta}$ = −26.3 kJ·mol^{-1}
$\Delta\rho_{3,\beta}$ = −0.16 $\psi^2_{-3,\beta}$ + 0.16 $\psi^2_{+3,\beta}$

Figure S48. Deformation densities of **PdSiAr^{Mes}**.

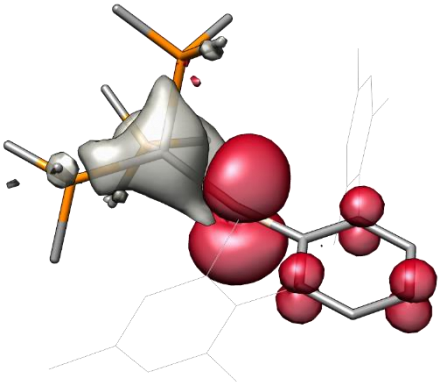

SOMO(SiAr^{Mes})→SOMO(Pt(PMe$_3$)$_3^+$)
$\Delta E_{orb,1,\alpha} = -172.4$ kJ·mol^{-1}
$\Delta\rho_{1,\alpha} = -0.87\ \psi^2_{-1,\alpha} + 0.87\ \psi^2_{+1,\alpha}$

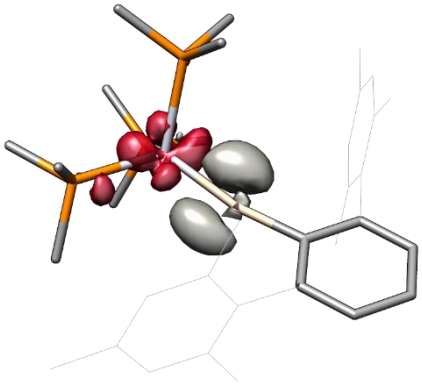

HOMO−3(Pt(PMe$_3$)$_3^+$)→LUMO(SiAr^{Mes})
$\Delta E_{orb,2,\alpha} = -56.0$ kJ·mol^{-1}
$\Delta\rho_{2,\alpha} = -0.30\ \psi^2_{-2,\alpha} + 0.30\ \psi^2_{+2,\alpha}$

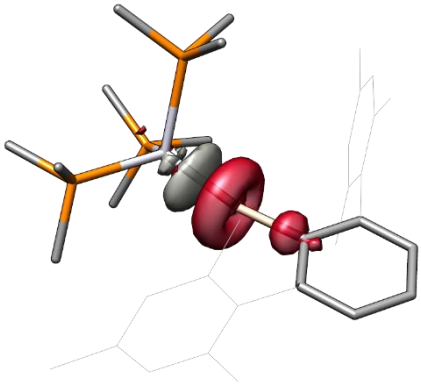

HOMO(SiAr^{Mes})→LUMO(Pt(PMe$_3$)$_3^+$)
$\Delta E_{orb,3,\alpha} = -52.0$ kJ·mol^{-1}
$\Delta\rho_{3,\alpha} = -0.23\ \psi^2_{-3,\alpha} + 0.23\ \psi^2_{+3,\alpha}$

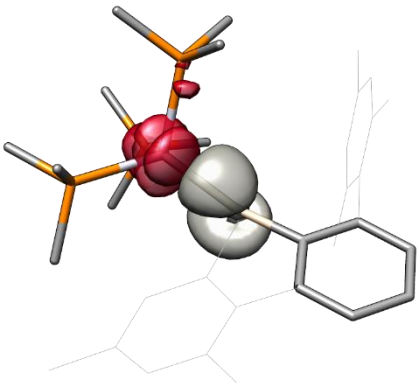

SOMO(Pt(PMe$_3$)$_3^+$)→SOMO(SiAr^{Mes})
$\Delta E_{orb,1,\beta} = -79.3$ kJ·mol^{-1}
$\Delta\rho_{1,\beta} = -0.41\ \psi^2_{-1,\beta} + 0.41\ \psi^2_{+1,\beta}$

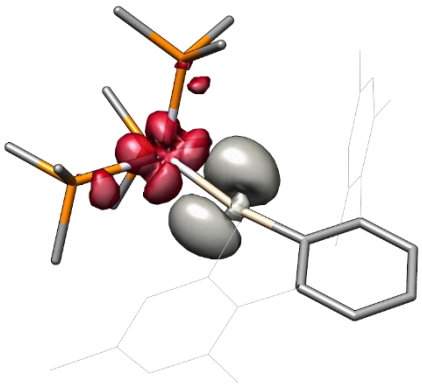

HOMO−3(Pt(PMe$_3$)$_3^+$)→LUMO(SiAr^{Mes})
$\Delta E_{orb,2,\beta} = -76.1$ kJ·mol^{-1}
$\Delta\rho_{2,\beta} = -0.36\ \psi^2_{-2,\beta} + 0.36\ \psi^2_{+2,\beta}$

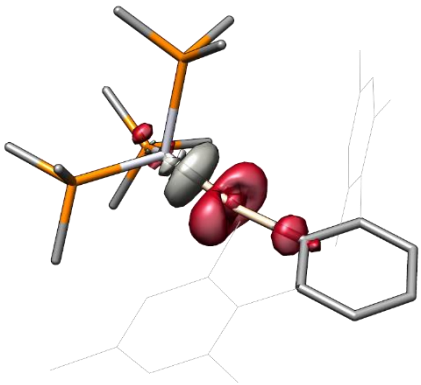

HOMO(SiAr^{Mes})→LUMO(Pt(PMe$_3$)$_3^+$)
$\Delta E_{orb,3,\beta} = -50.5$ kJ·mol^{-1}
$\Delta\rho_{3,\beta} = -0.22\ \psi^2_{-3,\beta} + 0.22\ \psi^2_{+3,\beta}$

Figure S49. Deformation densities of **PtSiAr^{Mes}**.

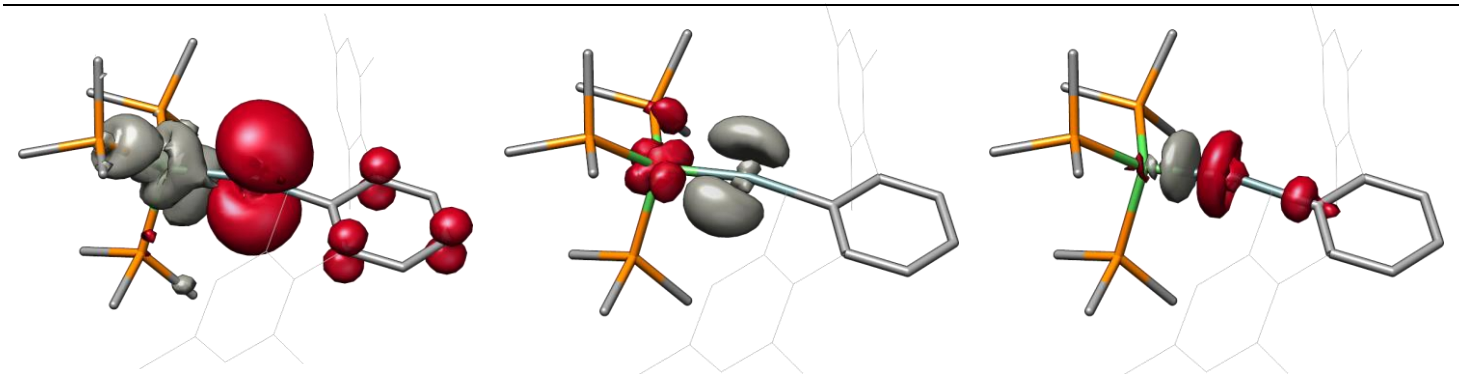

SOMO(GeAr^{Mes})→SOMO(Ni(PMe$_3$)$_3^+$)
$\Delta E_{orb,1,\alpha} = -108.4$ kJ·mol^{-1}
$\Delta\rho_{1,\alpha} = -0.87\ \psi^2_{-1,\alpha} + 0.87\ \psi^2_{+1,\alpha}$

HOMO(Ni(PMe$_3$)$_3^+$)→LUMO(GeAr^{Mes})
$\Delta E_{orb,2,\alpha} = -59.4$ kJ·mol^{-1}
$\Delta\rho_{2,\alpha} = -0.33\ \psi^2_{-2,\alpha} + 0.33\ \psi^2_{+2,\alpha}$

HOMO−1(GeAr^{Mes})→LUMO(Ni(PMe$_3$)$_3^+$)
$\Delta E_{orb,3,\alpha} = -38.1$ kJ·mol^{-1}
$\Delta\rho_{3,\alpha} = -0.18\ \psi^2_{-3,\alpha} + 0.18\ \psi^2_{+3,\alpha}$

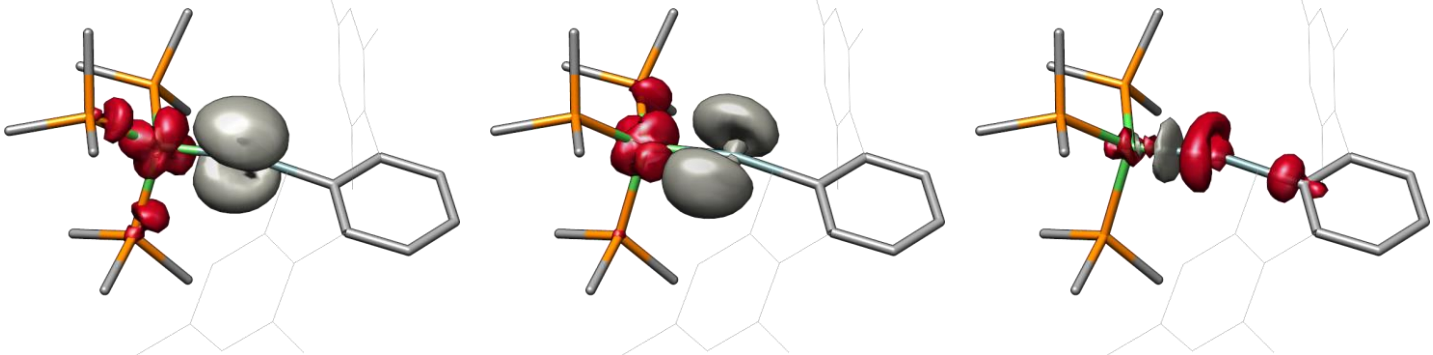

SOMO(Ni(PMe$_3$)$_3^+$)→SOMO(GeAr^{Mes})
$\Delta E_{orb,1,\beta} = -71.2$ kJ·mol^{-1}
$\Delta\rho_{1,\beta} = -0.41\ \psi^2_{-1,\beta} + 0.41\ \psi^2_{+1,\beta}$

HOMO(Ni(PMe$_3$)$_3^+$)→LUMO(GeAr^{Mes})
$\Delta E_{orb,2,\beta} = -76.3$ kJ·mol^{-1}
$\Delta\rho_{2,\beta} = -0.38\ \psi^2_{-2,\beta} + 0.38\ \psi^2_{+2,\beta}$

HOMO−1(GeAr^{Mes})→LUMO(Ni(PMe$_3$)$_3^+$)
$\Delta E_{orb,3,\beta} = -39.3$ kJ·mol^{-1}
$\Delta\rho_{3,\beta} = -0.18\ \psi^2_{-3,\beta} + 0.18\ \psi^2_{+3,\beta}$

Figure S50. Deformation densities of **NiGeAr^{Mes}**.

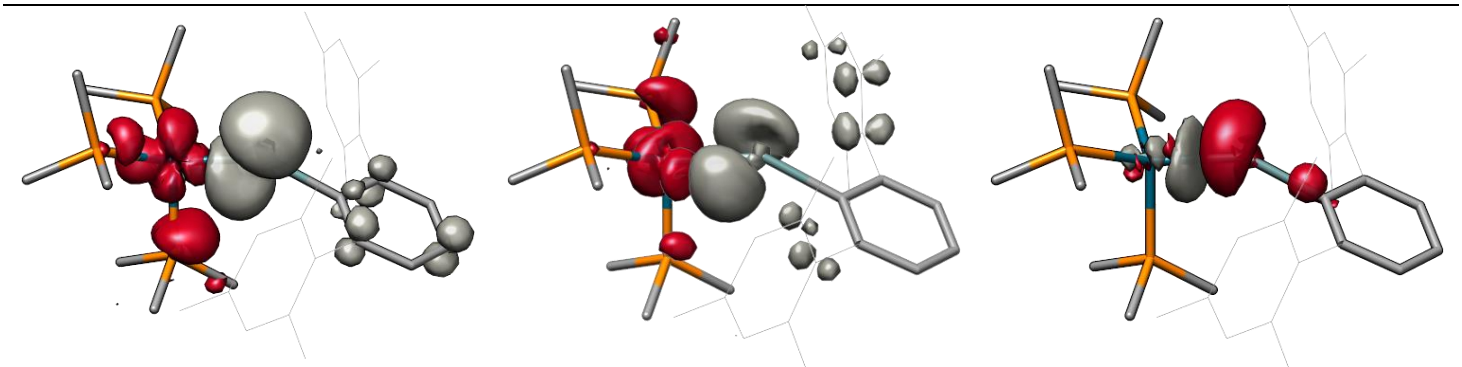

HOMO−1(Pd(PMe$_3$)$_3$)→LUMO+1(GeAr^{Mes+})
$\Delta E_{orb,1} = -208.5$ kJ·mol^{-1}
$\Delta\rho_1 = -0.81\ \psi^2_{-1} + 0.81\ \psi^2_{+1}$

HOMO(Pd(PMe$_3$)$_3$)→LUMO(GeAr^{Mes+})
$\Delta E_{orb,2} = -144.3$ kJ·mol^{-1}
$\Delta\rho_2 = -0.70\ \psi^2_{-2} + 0.70\ \psi^2_{+2}$

HOMO−10(GeAr^{Mes+})→LUMO(Pd(PMe$_3$)$_3$)
$\Delta E_{orb,3} = -36.6$ kJ·mol^{-1}
$\Delta\rho_3 = -0.30\ \psi^2_{-3} + 0.30\ \psi^2_{+3}$

Figure S51. Deformation densities of **PdGeAr^{Mes}**.

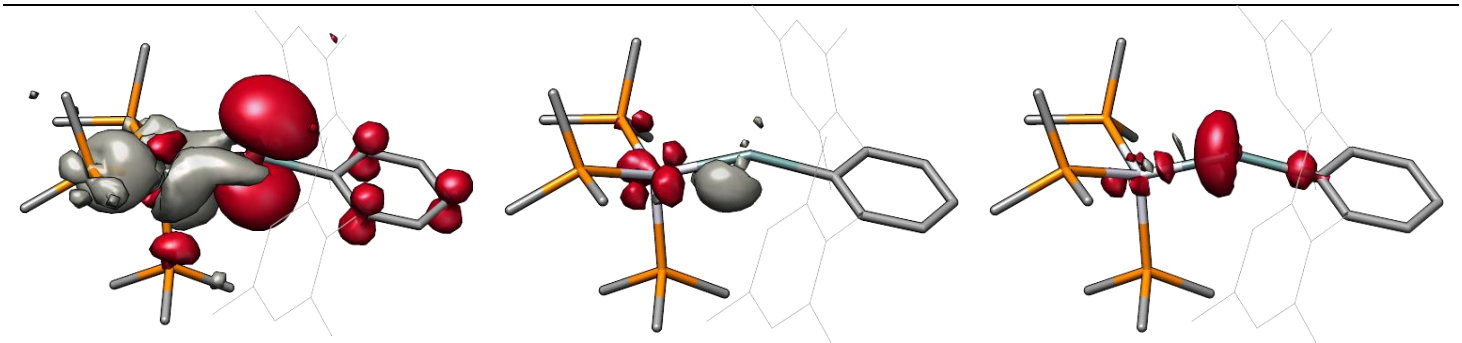

SOMO(GeAr^{Mes})→SOMO(Pt(PMe$_3$)$_3^+$)
$\Delta E_{orb,1,\alpha} = -202.5$ kJ·mol^{-1}
$\Delta\rho_{1,\alpha} = -0.92\ \psi^2_{-1,\alpha} + 0.92\ \psi^2_{+1,\alpha}$

HOMO(Pt(PMe$_3$)$_3^+$)→LUMO(GeAr^{Mes})
$\Delta E_{orb,2,\alpha} = -31.6$ kJ·mol^{-1}
$\Delta\rho_{2,\alpha} = -0.23\ \psi^2_{-2,\alpha} + 0.23\ \psi^2_{+2,\alpha}$

HOMO−1(GeAr^{Mes})→LUMO(Pt(PMe$_3$)$_3^+$)
$\Delta E_{orb,3,\alpha} = -41.5$ kJ·mol^{-1}
$\Delta\rho_{3,\alpha} = -0.20\ \psi^2_{-3,\alpha} + 0.20\ \psi^2_{+3,\alpha}$

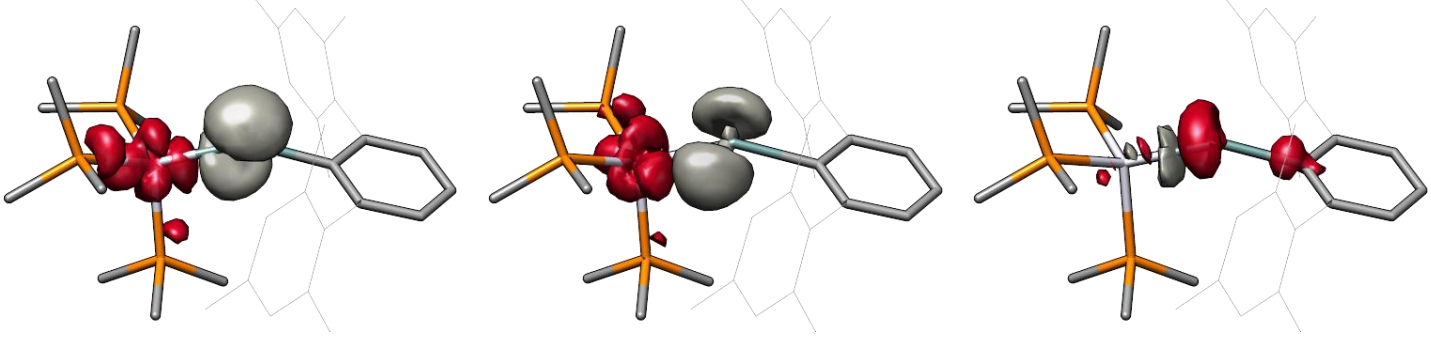

SOMO(Pt(PMe$_3$)$_3^+$)→SOMO(GeAr^{Mes})
$\Delta E_{orb,1,\beta} = -74.9$ kJ·mol^{-1}
$\Delta\rho_{1,\beta} = -0.40\ \psi^2_{-1,\beta} + 0.40\ \psi^2_{+1,\beta}$

HOMO(Pt(PMe$_3$)$_3^+$)→LUMO(GeAr^{Mes})
$\Delta E_{orb,2,\beta} = -61.5$ kJ·mol^{-1}
$\Delta\rho_{2,\beta} = -0.35\ \psi^2_{-2,\beta} + 0.35\ \psi^2_{+2,\beta}$

HOMO−1(GeAr^{Mes})→LUMO(Pt(PMe$_3$)$_3^+$)
$\Delta E_{orb,3,\beta} = -41.2$ kJ·mol^{-1}
$\Delta\rho_{3,\beta} = -0.20\ \psi^2_{-3,\beta} + 0.20\ \psi^2_{+3,\beta}$

Figure S52. Deformation densities of **PtGeAr^{Mes}**.

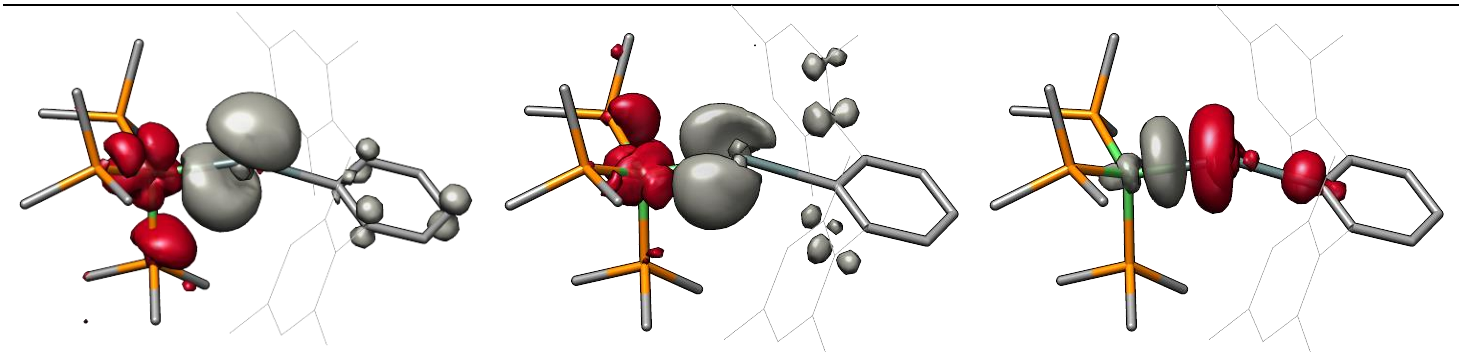

HOMO−1(Ni(PMe$_3$)$_3$)→LUMO+1(SnAr^{Mes+})
$\Delta E_{orb,1} = -185.0$ kJ·mol^{-1}
$\Delta\rho_1 = -0.79\ \psi^2_{-1} + 0.79\ \psi^2_{+1}$

HOMO(Ni(PMe$_3$)$_3$)→LUMO(SnAr^{Mes+})
$\Delta E_{orb,2} = -136.3$ kJ·mol^{-1}
$\Delta\rho_2 = -0.67\ \psi^2_{-2} + 0.67\ \psi^2_{+2}$

HOMO−6(SnAr^{Mes+})→LUMO(Ni(PMe$_3$)$_3$)
$\Delta E_{orb,3} = -42.9$ kJ·mol^{-1}
$\Delta\rho_3 = -0.32\ \psi^2_{-3} + 0.32\ \psi^2_{+3}$

Figure S53. Deformation densities of **NiSnAr^{Mes}**.

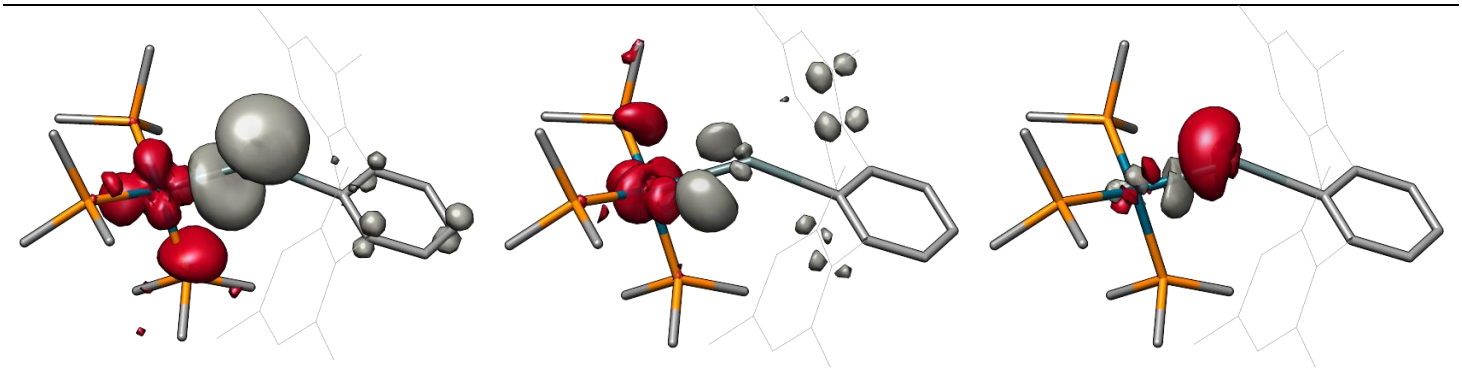

HOMO−4(Pd(PMe$_3$)$_3$)→LUMO+1(SnAr^{Mes+})
$\Delta E_{orb,1}$ = −183.5 kJ·mol^{-1}
$\Delta\rho_1 = -0.77\ \psi^2_{-1} + 0.77\ \psi^2_{+1}$

HOMO−3(Pd(PMe$_3$)$_3$)→LUMO(SnAr^{Mes+})
$\Delta E_{orb,2}$ = −93.0 kJ·mol^{-1}
$\Delta\rho_2 = -0.57\ \psi^2_{-2} + 0.57\ \psi^2_{+2}$

HOMO−6(SnAr^{Mes+})→LUMO(Pd(PMe$_3$)$_3$)
$\Delta E_{orb,3}$ = −27.2 kJ·mol^{-1}
$\Delta\rho_3 = -0.25\ \psi^2_{-3} + 0.25\ \psi^2_{+3}$

Figure S54. Deformation densities of **PdSnAr^{Mes}**.

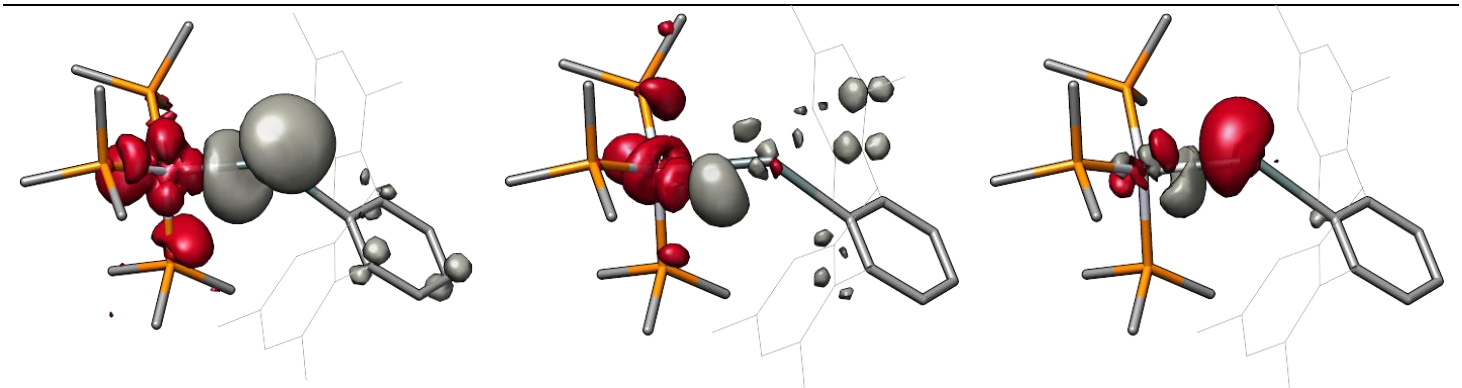

HOMO−4(Pt(PMe$_3$)$_3$)→LUMO+1(SnAr^{Mes+})
$\Delta E_{orb,1}$ = −198.5 kJ·mol^{-1}
$\Delta\rho_1 = -0.79\ \psi^2_{-1} + 0.79\ \psi^2_{+1}$

HOMO−3(Pt(PMe$_3$)$_3$)→LUMO(SnAr^{Mes+})
$\Delta E_{orb,2}$ = −98.3 kJ·mol^{-1}
$\Delta\rho_2 = -0.57\ \psi^2_{-2} + 0.57\ \psi^2_{+2}$

HOMO−6(SnAr^{Mes+})→LUMO(Pt(PMe$_3$)$_3$)
$\Delta E_{orb,3}$ = −38.4 kJ·mol^{-1}
$\Delta\rho_3 = -0.31\ \psi^2_{-3} + 0.31\ \psi^2_{+3}$

Figure S55. Deformation densities of **PtSnAr^{Mes}**.

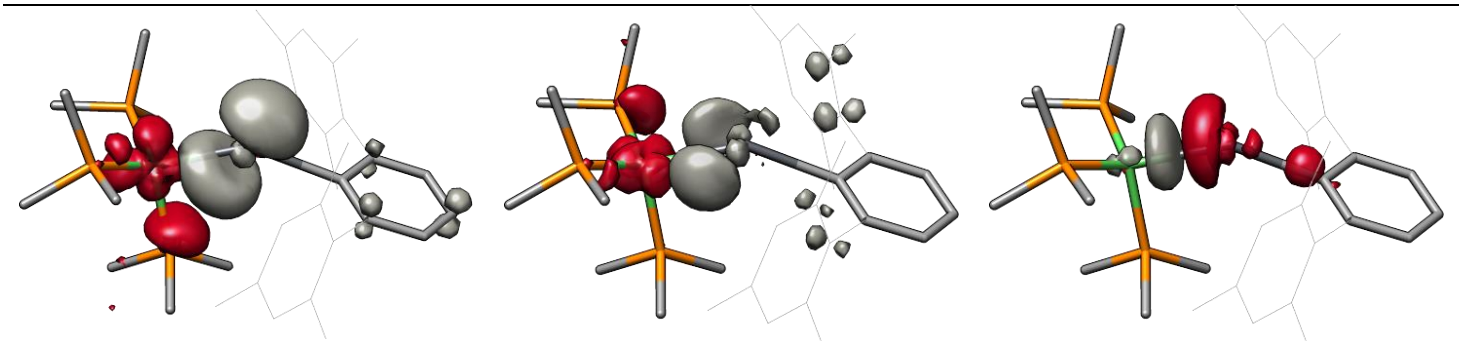

HOMO(Ni(PMe$_3$)$_3$)→LUMO+1(PbAr^{Mes+})
$\Delta E_{orb,1}$ = −175.9 kJ·mol^{-1}
$\Delta\rho_1 = -0.76\ \psi^2_{-1} + 0.76\ \psi^2_{+1}$

HOMO−1(Ni(PMe$_3$)$_3$)→LUMO(PbAr^{Mes+})
$\Delta E_{orb,2}$ = −113.7 kJ·mol^{-1}
$\Delta\rho_2 = -0.62\ \psi^2_{-2} + 0.62\ \psi^2_{+2}$

HOMO−5(PbAr^{Mes+})→LUMO(Ni(PMe$_3$)$_3$)
$\Delta E_{orb,3}$ = −34.3 kJ·mol^{-1}
$\Delta\rho_3 = -0.27\ \psi^2_{-3} + 0.27\ \psi^2_{+3}$

Figure S56. Deformation densities of **NiPbAr^{Mes}**.

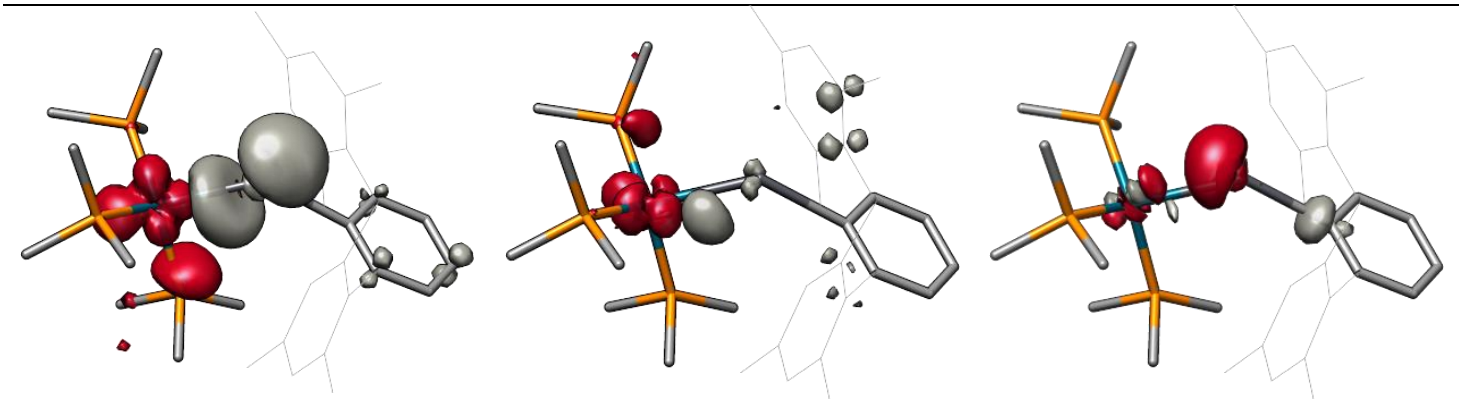

HOMO−4(Pd(PMe$_3$)$_3$)→LUMO+1(PbAr^{Mes+})
$\Delta E_{orb,1}$ = −170.4 kJ·mol^{-1}
$\Delta\rho_1 = -0.74\ \psi^2_{-1} + 0.74\ \psi^2_{+1}$

HOMO−3(Pd(PMe$_3$)$_3$)→LUMO(PbAr^{Mes+})
$\Delta E_{orb,2}$ = −71.2 kJ·mol^{-1}
$\Delta\rho_2 = -0.50\ \psi^2_{-2} + 0.50\ \psi^2_{+2}$

HOMO−6(PbAr^{Mes+})→LUMO(Pd(PMe$_3$)$_3$)
$\Delta E_{orb,3}$ = −20.8 kJ·mol^{-1}
$\Delta\rho_3 = -0.21\ \psi^2_{-3} + 0.21\ \psi^2_{+3}$

Figure S57. Deformation densities of **PdPbAr^{Mes}**.

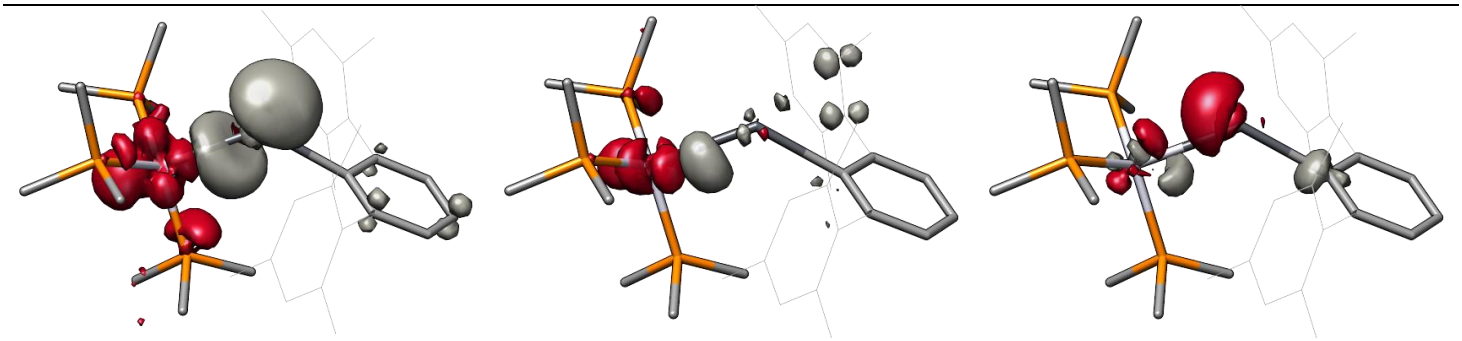

HOMO−4(Pt(PMe$_3$)$_3$)→LUMO+1(PbAr^{Mes+})
$\Delta E_{orb,1}$ = −180.1 kJ·mol^{-1}
$\Delta\rho_1 = -0.76\ \psi^2_{-1} + 0.76\ \psi^2_{+1}$

HOMO−3(Pt(PMe$_3$)$_3$)→LUMO(PbAr^{Mes+})
$\Delta E_{orb,2}$ = −74.7 kJ·mol^{-1}
$\Delta\rho_2 = -0.50\ \psi^2_{-2} + 0.50\ \psi^2_{+2}$

HOMO−6(PbAr^{Mes+})→LUMO(Pt(PMe$_3$)$_3$)
$\Delta E_{orb,3}$ = −26.8 kJ·mol^{-1}
$\Delta\rho_3 = -0.25\ \psi^2_{-3} + 0.25\ \psi^2_{+3}$

Figure S58. Deformation densities of **PtPbAr^{Mes}**.

13) Metallotetrylene isomers **MER-2** as found by PES scans

Table S11. Key properties of metallotetrylene isomers **MER-2** derived from the **MER** complexes. ΔE_{rel} is the energy difference at level of theory **II** (E(**MER-2**) – E(**MER**)). No **MER-2** isomer could be obtained for **NiSiTbb** and **NiSiAr^{Mes}**.

compound	ΔE_{rel}	MER			MER-2		
		M–E	E–C1	M–E–C1	M–E	E–C1	M–E–C1
NiSiTbb	/	204.5	184.0	167.2	/	/	/
NiSiAr^{Mes}	/	204.2	185.6	167.4	/	/	/
NiGeAr^{Mes}	83.5	213.3	197.1	165.3	235.9	204.0	95.1
NiSnAr^{Mes}	55.3	235.1	219.4	150.9	256.3	224.3	96.0
NiPbAr^{Mes}	36.4	244.9	229.7	142.7	264.2	234.3	94.8
PdSiTbb	47.1	215.1	184.0	163.1	235.1	189.7	98.8
PdSiAr^{Mes}	28.7	216.1	187.6	150.7	232.4	191.0	87.9
PdGeAr^{Mes}	1.5	227.9	199.5	144.9	246.4	202.7	90.6
PdSnAr^{Mes}	−17.6	251.6	222.9	134.4	270.3	223.6	93.1
PdPbAr^{Mes}	−25.3	263.1	232.4	129.6	277.4	232.7	93.6
PtSiTbb	78.4	215.8	183.8	168.1	239.0	191.0	101.0
PtSiAr^{Mes}	41.8	215.7	183.6	166.1	238.1	192.5	100.0
PtGeAr^{Mes}	7.4	228.4	198.9	149.7	250.7	204.0	98.7
PtSnAr^{Mes}	−13.7	255.1	223.9	132.1	274.3	225.4	96.9
PtPbAr^{Mes}	−28.5	267.7	233.1	127.3	281.9	233.7	94.3

14) References

1. Okuniewski, A.; Rosiak, D.; Chojnacki, J.; Becker, B. Coordination Polymers and Molecular Structures among Complexes of Mercury(II) Halides with Selected 1-Benzoylthioureas. *Polyhedron* **2015**, *90*, 47–57, doi:10.1016/j.poly.2015.01.035.

2. Keil, P.M.; Hadlington, T.J. Accessing Cationic Tetrylene-Nickel(0) Systems Featuring Donor–Acceptor E–Ni Triple Bonds (E = Ge, Sn). *Chem. Commun.* **2022**, 3011, doi:10.1039/D2CC00422D.